POLITECNICO DI TORINO

Collegio di Ingegneria Meccanica

Corso di Laurea in Ingegneria Meccanica

Tesi di Laurea Magistrale

Sintering and microstructure analysis of rapidly cooled alloys

Relatore:

FERRARIS MONICA

Correlatore:

SHARIFIKOLOUEI ELHAM

Candidato:

XINGSHANG

Anno Accademico 2020 - 2021

CONTENTS

Abstract **1**

1. Introduction **2**

1.1 Bulk metallic glasses 2
1.2 Classification of iron-based metallic glasses 4
1.3 Mechanical properties for iron-based bulk metallic glasses 5
1.4 Effect of composition on their properties 7
1.5 Effect of heat treatment on their properties 8
1.6 Applications 10

2. Materials and methods **11**

2.1 Materials preparation 11
2.2 Sample preparation 12
2.3 Sample thermal treatment 13
2.4 Structural analysis 13
2.5 Thermal properties 14

3. Results and discussion **16**

3.1 Microstructure analysis 16
3.2 DSC data evaluation 21
3.3 XRD data evaluation 25

4. Conclusions **31**

Abbreviations **32**

List of Figures **33**

List of Tables **35**

References **36**

Acknowledgments **48**

Abstract

Fe-based bulk metallic glasses (BMGs) have been extensively studied due to their potential technological applications and their interesting physical and mechanical properties such as a low modulus of elasticity, high yielding stress and good magnetic properties. In the present work, master alloys with nominal compositions of $Fe_{80}Si_5B_{15}$, $Fe_{72}B_{19}Si_5Nb_4$, and $Fe_{40}Ni_{40}B_{20}$ (numbers indicate at. %) were prepared by arc melting the constituent elements in a Ti-gettered Argon atmosphere. The ingots were further used to fabricate metallic glass microfibers by the recently developed modified melt-spinning technique. The influence of sintering on crystallization behavior, microstructure of the $Fe_{80}Si_5B_{15}$, $Fe_{72}B_{19}Si_5Nb_4$, and $Fe_{40}Ni_{40}B_{20}$ (numbers indicate at. %) samples was investigated while the effect of Si and Nb alloying additions on the crystallization of Fe–Si–B based alloys was also studied. The thermal properties associated with crystallization temperature of the glassy samples were measured using differential scanning calorimetry (DSC) at a heating rate of 20°C/min. The microstructure and phase formation of the samples have been analyzed by using X-ray diffractometry (XRD) and Scanning Electron Microscopy (SEM).

1. Introduction

1.1 Bulk metallic glasses

Crystalline materials are usually composed of grains with different sizes and specific microstructures. Therefore, they contain many crystalline defects such as dislocations and grain boundaries. The movement of dislocations under load will cause plastic deformation of crystalline materials, which is the reason why crystalline alloys cannot achieve the theoretical strength needed to break the atomic bonds. However, grain boundaries tend to promote corrosion and / or chemical reactions (for instance, oxidation and sulfidation). Therefore, mechanical properties of crystalline materials strongly depend on their crystalline structures. The atomic origins of the strength and ductility of crystalline materials can be explained by the well-established dislocation theory [1]. The limitations of crystalline materials structures can be changed through the formation of a glassy structure with randomly-packed atoms, generally called metallic glasses. Unlike the crystalline alloys, amorphous solids, such as metallic glasses, lack long-range order characteristics [2,3]. The disordered structure and metastable state make metallic glasses exhibit unusual structural properties and non-conventional deformation mechanisms [4,5]. In fact, some amorphous materials (i.e., polymers, glasses, and plastics) have been applied widely to our daily life. However, amorphous metallic alloys represent a relatively-new class of materials, compared to other amorphous materials [4]. Before 1960, only amorphous thin films were successfully deposited at very low temperatures [6]. An amorphous alloy was first synthesized in 1960 through rapidly-quenching an Au-Si alloy directly with rates up to 106 K/s [6]. The significance of the work is that the process of the nucleation and growth of crystalline phases could be kinetically bypassed in some molten alloys to produce metallic glasses. However, the specimen geometry was severely restricted to thin ribbons, foils, and powders, because the high rate of heat transfer was required to prevent crystallization at that time. Since then, remarkable progress was made in exploring alloy compositions for excellent glass formers with ever-lower critical cooling rates. In the late 1980s, Inoue's group discovered new multicomponent bulk-metallic-glass (BMG) systems with lower critical cooling rates and thicknesses of several millimeters [7,8]. A family of multicomponent Zr-based BMGs (e.g., Zr-Cu-Ni and Zr-Cu-Ni-Al BMGs) were also developed later [7–9]. Moreover, Peker and Johnson developed a quinary alloy, Zr-Ti-Cu-Ni-Be, with lower critical cooling rates down to 1 K/s in 1993 [10]. The alloy, $Zr_{41.2}Cu_{12.5}Ni_{10}Ti_{13.8}Be_{22.5}$ (in atomic percent, at. %), was the first commercial BMG and named as Vitreloy 1 (Vit 1) [3]. Since then, a vast number of glass-forming alloy systems were greatly developed, for example, binary, ternary, and multi-component alloy systems. These metallic-glass alloy systems involved Al-, Cu-, Fe-, La-, Mg-, Ni-, Pd-, Ti-, and Zr-based alloys [11–28].

Owing to the fact that they lack microstructural features, such as grains, grain boundaries, and dislocations, BMGs display many excellent properties: high strengths (even an ultra-high strength of over 5 GPa); high hardness; high strength to weight ratios; superior elastic limits; low coefficients of frictions; high scratch and wear resistances; good corrosion resistances; net-shape castability; and good soft magnetic behavior [29–35]. BMGs have been used to produce many products, for example: sporting goods, watch parts, electromagnetic casings, optical parts, ornamental parts, choke coils, power inductors, magnetic-field-identification systems, electromagnetic-wave-shielding sheets, micro-geared motor parts, pressure sensors, surface-coating materials, and medical instruments [2].

Nevertheless, the excellent properties of BMGs are accompanied by their lack of homogeneous plastic deformation without dislocation-mediated crystallographic slip [5]. Inhomogeneous deformation, in general, happens in BMGs under the unconstrained conditions because of the formation and propagation of highly-localized shear bands where a high amount of plastic strains is accumulated in a very narrow region (i.e., 10–20 nm) [4,36–38]. Although plastic strains are very large at the localized shear bands, the overall plastic deformability of BMGs at low temperatures is disappointingly low (< 2–3%) [36]. Therefore, this kind of brittleness seriously confines the applications of BMGs as a potential candidate for engineering and structural materials.

Extensive experimental studies using a wide variety of characterization techniques have been utilized to elucidate the microstructural root cause of the brittleness in BMGs. A few important ones include the mechanical heterogeneity characterization with nanoindentation [39,40] and dynamic force microscopy [41], morphological analysis of fracture surfaces with scanning electron microscopy (SEM) and atomic force microscopy (AFM) [42,43], and systematic measurements of Poisson's ratio and the ratio of the elastic shear modulus to the bulk modulus [44,45]. At the same time, various theoretical models based on atomic operations were proposed and used for exploring deformation mechanisms in metallic glasses. One of such models is the free volume model, which models the inhomogeneous deformation in metallic glasses as a result of the biased accumulation of free volumes at certain locations under the action of stress [46–49]. Another commonly used model is the shear transformation zone (STZ) model, which treats clusters of atoms as the carriers of plastic deformation in metallic glasses. The STZ model was originally proposed by Argon [50] and later elaborated by Langer and Falk [51,52], and has been widely used in molecular dynamics simulations of deformation and failure processes in metallic glasses [51–54]. For interpreting the quasi-cleavage fracture features observed in BMGs, the tension transformation zone (TTZ) model may find more usages [55]. TTZs are also local clusters of atoms, their size is like STZs, but the relaxation timescales are reduced, and brittle fracture is more likely to occur when subjected to loads. Recently, realizing that metallic glasses may contain a great number of structural heterogeneities, a flow unit mode was proposed to study the inhomogeneous nature of metallic glasses [49]. Flow units are essentially loosely packed regions inside an elastic metallic glass matrix, possess low modulus and strength, and behave like viscous liquids.

1.2 Classification of iron-based metallic glasses

Materials scientists have developed some iron-based amorphous alloy systems from the aspects of alloy composition, preparation process and application performance. The following is the main classification of iron-based metallic glasses. [143]

A . Iron-based metallic glasses

The main components of iron-based amorphous alloys are Fe, Si, and B. For example, $Fe_{80}Si_5B_{15}$. It is characterized by strong magnetism, better soft magnetic properties, and low cost. It is most suitable for replacing electrical steel sheets and it is used as the iron core of low frequency transformers.

B. Iron-nickel-based metallic glasses

The main components of Iron-nickel-based amorphous alloys are Fe, Ni, Si, B. For example, $Fe_{40}Ni_{40}B_{20}$. It is characterized by relatively weak magnetism, but relatively high magnetic permeability, and expensive. It is most suitable for replacing permalloy and it is used as the iron core of high-demand medium and low frequency transformers.

C. Iron-based nanocrystalline alloys (ultra-microcrystalline alloys)

The main components of iron-based nanocrystalline alloys are Fe, Si, B and a small amount of Cu, Mo, Nb, etc., among which Cu and Nb are essential elements for obtaining nanocrystalline structures. For example, $Fe_{72}B_{19}Si_5Nb_4$. They are first made into amorphous materials, and then appropriately annealed to form a mixed structure of microcrystalline and amorphous. This type of alloy combines the high magnetic induction of iron-based amorphous alloys and the high permeability and low loss of iron-cobalt-based amorphous alloys. It is a low-cost iron-based material. It can replace microcrystalline permalloy and ferrite, and has been widely used in the fields of high-frequency power electronics to achieve the purpose of reducing size and cost.

D. Iron-cobalt-based metallic glasses

The main components of Iron-cobalt-based amorphous alloys are Co, Fe, Si, and B. It is characterized by weak magnetism. However, the magnetic permeability is extremely high and the price is very expensive. It generally replaces permalloy and ferrite, and it is used for transformers and inductors in demanding military power supplies.

1.3 Mechanical properties for iron-based bulk metallic glasses

Traditional iron-based MGs are usually formed as ribbons, powder or wires, and they can be prepared by chilling metallic liquids at a critical cooling rate above 106 K/s. The earliest iron-based MG can be traced back to 1967 when amorphous Fe-P-C alloys were invented by Duwez and his co-workers [56]. Compared with traditional silicon steels, these iron-based MGs exhibited broad application prospects due to their cheaper production cost, higher saturation magnetization, lower coercive force, and lower core loss, which fulfilled the increasing requirements of high-performance soft magnetic materials for energy saving. In consequence, much research has been devoted to searching for new iron-based MGs with improved soft magnetic properties. Subsequently, numerous iron-based MGs such as Fe-P-B [57], (Fe, Co, Ni)-Si-B [58], (Fe, Co, Ni)-Mo-C [59] and (Fe, Co, Ni)-M-B (M = Zr, Hf, Nb) [60] were developed. In particular, the Fe-Co-P-B and the Fe-Co-Si-B amorphous alloys, named “METGLAS”, have been widely commercialized [61]. In 1988, Yoshizawa et al. discovered that the soft magnetic properties of Fe-Si-B MGs could be significantly enhanced by Cu and Nb alloying, coupled with annealing treatments, which finally led to the birth of the FINEMET alloy (the famous brand of soft magnetic Fe-based MG ribbons) [62]. Afterwards, Fe-Zr-B, Fe-Hf-B and Fe-M-B-Cu (M = Ti, Zr, Hf, Nb, or Ta) MGs were also developed and named NANOPERM alloys [63]. Later, the (Fe, Co)-M-B-Cu (M = Nb, Hf, or Zr) nanocrystalline alloys, called HITPERM alloys, were also invented [64]. Currently, these commercial FINEMET, NANOPERM and HITPERM alloys are still widely applied in industries due to their excellent soft magnetic properties [64]. However, the low GFA makes the thickness of these Fe-based MG ribbons less than 50 µm, which results in the low packing density of the transformer core and then increases the Joule losses [65]. In order to reduce this energy loss, the thickness of the iron-based MG ribbon needs to be increased, that is, their GFA must be significantly improved.

Regarding the birth of iron-based BMGs, If the millimeter scale or low critical cooling rate (≤103 K/s) can be arbitrarily defined as “bulk”, the first Fe-based BMG, that is, $Fe_{73}Al_5Ga_2P_{11}C_5B_4$, was reported by Inoue and co-workers from Tohoku University, Japan, in 1995 [66]. Fig.1 exhibits the typical DSC curves and XRD patterns of the $Fe_{73}Al_5Ga_2P_{11}C_5B_4$ rods with different diameters fabricated by the injection casting method [66]. Obviously, a broad halo peak around $2\theta = 43.6°$ is observed on the XRD patterns, and the glass transition temperature and the onset temperature of crystallization show no obvious difference between these as-cast rods and as-spun ribbons, indicating their amorphous nature. Although from the current point of view, the GFA of this alloy is limited, nevertheless, its inception indeed opened a new avenue into the studies and applications of iron-based BMGs, which can inspire more researchers to engage in the development and application of iron-based metallic glass.

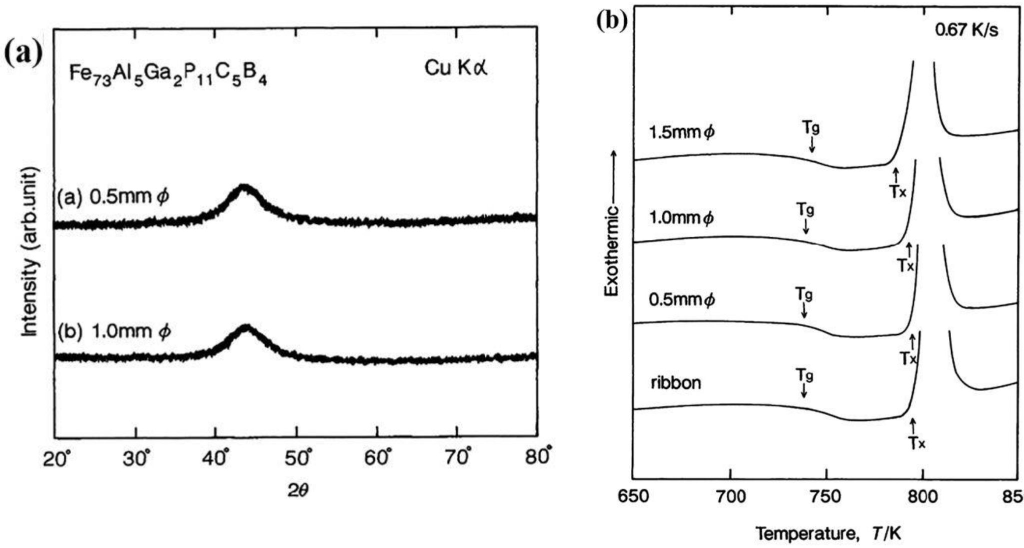

Figure. 1.1. Typical DSC curves and XRD patterns for the $Fe_{73}Al_5Ga_2P_{11}C_5B_4$ rods with different diameters fabricated by the injection casting method [66].

After Inoue's groundbreaking work in 1995, the search for large-sized iron-based BMGs became the main target of this field. Shortly, a series of Fe-based BMGs including Fe-(Nb, Cr, Mo)-(Al, Ga)-(P, B, C) [67], Fe-Co-(Zr, Hf, Nb)-(Mo, W)-B [68], Fe-Co-Nd-Dy-B [69], Fe-Co-Ga-(P, C, B) [70], Fe-(Co, Cr, Mo, Ga)-(P, C, B) [71], Fe-Ni-P-B [72], and Fe-B-Si-(Zr, Nb) [73] were fabricated with a critical diameter between 1 and 6 mm. Meanwhile, the fluxing treatment technique, which was originally applied to Pd-based alloys, was also used to improve the GFA of Fe-(Co, Cr, Mo, Ga, Sb)-C-B-P and Fe-Ni-P-B BMGs by Shen et al [72,74]. Until 2004, nevertheless, centimeter-sized iron-based BMGs were successfully developed independently by Poon et al. [75] and Lu et al. [76] via the addition of Er and Y, respectively. With continuous efforts, in 2013, the largest attainable size of full glass formation in Fe-based alloys was increased to 18 mm in the $(Fe_{0.8}Co_{0.2})_{47}Cr_{15}Mo_{14}C_{15}B_6Tm_3$ alloy [77]. So far, more than 10 kinds of centimeter-sized iron-based BMGs have been developed successfully. Additionally, it can be noticed that the largest GFA of iron-based BMGs (i.e.,18 mm) is still lower than those of Pd- [78], Zr- [79], Ti- [80], La- [81], Cu- [83], Mg- [84], Y- [85], Ni- [86], and Pt-based alloys [87] but higher than those of Ce- [82], Nd- [88], Ca- [89], Co- [90], Hf- [91], Sm- [92], Au- [93], Pr- [94], Zn- [95], and Al-based alloys [96]. Recently, by utilizing the Direct Metal Laser Sintering process (DMLS), a typical 3D printing technology, the critical size of Fe-Cr-Mo-C-B BMGs reached 45 mm, which exceeded the casting thickness of the material by a factor of > 15 [97]. Although a small number of sparsely distributed nanograin clusters were still observed in the amorphous matrix, there is no doubt that this result represents a new direction for manufacturing large-sized iron-based BMGs.

In addition, cost reduction has been another emphasis of research for enabling the widespread applications of Fe-based BMGs in the past few decades. In this aspect, several approaches have been proposed, including: 1. fabricating Fe-based BMGs using industrial raw materials, 2. minimizing the total amount of alloying elements, 3. excluding expensive RE elements, and 4. fabricating Fe-based BMGs under low vacuum conditions or even in air without any inert gas protection. Apparently, the usage of industrial raw materials tends to decrease the GFA due to the negative role of contained impurities [98]. Therefore, studying the influence of impurities on the GFA and its properties is very significant for the development of low-cost iron-based BMGs. Another successful example of reducing the cost of iron-based BMGs is the invention of the $Fe_{69.9}C_{7.1}Si_{3.3}B_{5.5}P_{8.7}Mo_{2.5}Al_{2.0}Co_{1.0}$ alloy, whose critical size reached 7 mm with no expensive RE elements [76]. Although some progress has been made, it still needs to be adjusted continuously along this line in the future, but this also sets the basic idea for the future development of iron-based metallic glass. It is believed that more new iron-based metallic glasses will be developed in the future.

In addition to the critical size and cost discussed above, another area of focus is to enhance the performance of iron-based BMGs. For non-magnetic applications, the brittleness at room temperature has consistently been a bottleneck for the widespread industrial application of iron-based BMGs. Unlike other BMGs such as Zr-based BMGs, the iron-based BMGs exhibit ceramic-like fracture behavior and the rods are normally pulverized under loading. Hence, many efforts have been devoted to uncovering the mechanism of the brittle fracture of iron-based BMGs and exploring reliable methods for improving their plasticity. Approaches such as creating composite microstructures, adjusting the nature of atomic bonding in the glass structure, properly controlling the intrinsic elastic properties, and geometric confinement, have been proven to be effective, to a certain degree, in improving the mechanical properties of iron-based BMGs [99–124]. Moreover, their large corrosion resistance, good wear resistance, high hardness, ion irradiation resistance, and decent catalytic properties have been intensively noticed in the past decades for their non-magnetic applications [77]. For the magnetic application, the methods used to overcome the dilemma between high saturation magnetization and large GFA, that is, developing iron-based BMGs with simultaneously large GFA and good soft magnetic properties, have consistently been a theme of research [125,126,127–135].

1.4 Effect of composition on their properties

Effects of alloying additions on glass formation, mechanical and soft-magnetic properties of Fe - (Si, P, C, B)-based bulk metallic glasses (BMGs) has been systemically studied in detail for recently years. For instance, Si and B are the metalloid elements more used to obtaining metallic glasses because they enhance the glass forming ability. On the other hand, it has been reported that relatively high content of Si (10 at. %) in Fe-Cr-Si-B alloy wires increase their mechanical strength [136]. In contrast, a subsequent investigation [137] stated that some iron-based amorphous wires with relatively low Si content (7.5 at. %) and high B (15 at. %) concentration have better mechanical properties. Further research shows that The Vickers microhardness increased as the B content was increased for all the series. On the other hand, the fracture strength, σ_{TS}, for $Fe_{82}Si_8B_{10}$ exhibited a gradual increase as a function of B contents. In contrast, σ_{ST} showed maximum values for $Fe_{80}Si_{10}B_{10}$ and $Fe_{70}Si_{10}B_{12}Cr_8$ at concentrations of 14 and 16 at.% B, respectively. In general, it was observed that the microhardness and strength of the alloy series with 8 at. % Si was higher compared with 10 at. % Si series. In addition, Cu-added iron-metalloid bulk glassy alloys exhibited excellent mechanical properties: a maximum stress of 3.3 GPa; a Young's modulus of 163 GPa, and a large plastic deformation of about 3.1% in compression [138]. The addition of too much Cu resulted in the enhancement of the size of nanoparticles but a decrease in glass-forming ability, which then led to a decrease in the critical diameter and the plasticity. This indicates that a Cu content within a certain range allows for nano-scale-iron of an appropriate size which then leads to the maximum values in plastic property [138]. Apart from these, The Cr addition in a large amount tends to decrease the glass forming ability since the liquidus temperature significantly increases with the increase of Cr content. However, corrosion resistance of the amorphous alloys increases as the Cr content increases leading to higher corrosion resistance of the amorphous alloy with 12.3 at% Cr content than the SUS304 alloy that contains much higher Cr and Ni contents. [139] Homogeneity as well as the Cr content of the passive layer plays an important role to protect the alloy from corrosive environments. The glass forming ability and the corrosion resistance of iron-based bulk metallic glass can be optimized for extensive practical applications through controlling the Cr content.

1.5 Effect of heat treatment on their properties

Heat treatment has an important influence on the properties of iron-based metallic glasses. In recent years, the research on the magnetic properties of iron-based metallic glasses by heat treatment has received extensive attention. For instance, by comparing the magnetic properties of $Fe_{80}Si_9B_{11}$ amorphous ribbons under different heat treatment processes, the variation law of magnetic properties was found, and the best annealing heat treatment system for magnetic properties was found: heating temperature 405 ℃, holding time 20 min [140]. Researchers compared the properties of samples before and after crystallization heat treatment, the effect of crystallization heat treatment on the properties of iron-based amorphous alloy was found: the corrosion resistance of amorphous ribbons before crystallization was high; the microhardness of amorphous ribbons after crystallization increased, but the brittleness increased significantly. In addition, the effects of annealing temperature and holding time of iron-based metallic glass prepared by a single-roll rapid quenching method in air on static magnetic properties and loss characteristics under AC low frequency are also studied. Through further research on $Fe_{57.6}Co_{14.4}B_{19.2}Si_{4.8}Nb_4$ metallic glass, the researchers found that as the annealing temperature increases, the maximum DC permeability increased, the coercivity decreased, and the resistivity increased. The best DC performance and AC low-frequency loss performance can be obtained by keeping the temperature at 773K for 30 minutes [141].

Furthermore, heat treatment also affected the crystallization behavior, the microstructure and the resulting micro-hardness of bulk metallic glass. For example, the $(Fe_{0.9}Ni_{0.1})_{77}Mo_5P_9C_{7.5}B_{1.5}$ which is an as-quenched bulk metallic glass (BMG) composite was investigated [142]. Researchers used DSC to anneal the amorphous composite material at different temperatures of T_{p1} (725 K) and T_{p2} (772 K), and studied the effect of crystallization of the amorphous composite on hardness by using XRD, SEM, EDS, DSC and micro-hardness test. Then, the researchers found that $(Fe_{0.9}Ni_{0.1})_{77}Mo_5P_9C_{7.5}B_{1.5}$ alloy shows liquid phase separation (LPHS) during solidification and possesses composite structure in as cast state. The experiment showed that both the separated phase and the matrix phase (L1 and L2) have high glass forming ability and show an amorphous structure in the as-cast state, each phase has different composition and so possesses different crystallization temperature and hardness. Finally, the researchers concluded that when annealing temperature raised up to 772 K (T_{p2}), the $Fe_{23}(C, B)_6$ and $FeNi_2P$ phases form in the matrix causing the hardness to increase, separated phase that was intensely crystallized with annealing at T_{p2} crystal structure was dominated, and the conditions become suitable for the growth of shear bands and cracks, resulting in a sharp decrease in hardness.

In addition to the effects mentioned above, the effect of heat treatment process on the electrochemical corrosion performance of iron-based amorphous alloys was also a research direction. For instance, the researchers first annealed the $Fe_{41}Co_7Cr_{15}Mo_{14}C_{15}B_6Y_2$ amorphous alloy prepared by vacuum arc melting copper mold casting technology and the $Fe_{41}Co_7Cr_{15}Mo_{14}C_{15}B_6Y_2$ amorphous alloy prepared by the amorphous crystallization annealing method. The annealing process was 610°C, 630°C, and 645°C respectively, and the holding time was 8h. The amorphous and their crystallization processes were identified by DSC and XRD. Then a comparative study of the electrochemical corrosion behaviors of amorphous $Fe_{41}Co_7Cr_{15}Mo_{14}C_{15}B_6Y_2$ alloys was performed by the electrochemical impedance spectroscopy (EIS) in 1.5 mol/l HCL solution and the influence of heat treatment at different temperatures on the alloy structure and corrosion resistance in 1.5 mol/l HCL solutions was investigated. Finally, the researchers found that at room temperature, in 1.5 mol/l HCl solution, the corrosion resistance of $Fe_{41}Co_7Cr_{15}Mo_{14}C_{15}B_6Y_2$ amorphous alloy was better than that of crystallized material and the corrosion current density was also relatively low. Moreover, with the increase of heat treatment temperature, the corrosion resistance of $Fe_{41}Co_7Cr_{15}Mo_{14}C_{15}B_6Y_2$ amorphous alloy decreased gradually.

1.6 Applications

Iron-based BMG has extremely high strength and toughness, a high elastic elongation limit, good corrosion resistance, and excellent soft magnetic properties. Since the first Fe-PC BMG was developed in 1995 [66], great strides have been made in exploring the industrial applications of these new materials in various fields, including soft magnetic applications, wear and corrosion resistant coatings, biomedical materials and precision gears for micromotors, shot peening balls, a fine precise polishing medium, catalysts, and so on. At present, iron-based BMG is mainly used as soft magnetic material and wear and corrosion resistant material coating. Recently, its applications have been extended to new areas such as biomaterials, shot peening balls, catalysts and amorphous electrical machinery. However, new applications of special types of glass alloys with many interesting properties should be explored to make the best use of their intrinsic properties.

2. Materials and Methods

2.1 Materials preparation

Master alloys with nominal compositions (at.%) of $Fe_{80}Si_5B_{15}$, $Fe_{72}B_{19}Si_5Nb_4$, and $Fe_{40}Ni_{40}B_{20}$ were prepared by arc melting the constituent elements in a Ti-gettered Argon atmosphere. The ingots were further used to fabricate metallic glass microfibers by the recently developed modified melt-spinning technique.[144]. The technique was used for microfiber fabrication at Academic Centre for Materials and Nanotechnology (ACMIN), at Prof. Bala's group in Krakow, Poland, receiving funding from KMM-VIN program. Figure 2.1. shows the schematic picture as well as optical picture of the technique and the prepared microfibers. The obtained microfibers had a diameter of about 1-2μm and tens of millimeters long. The composition and general properties of prepared microfibers are presented in Table 2.1. The as-cast samples were analyzed by SEM, XRD and DSC.

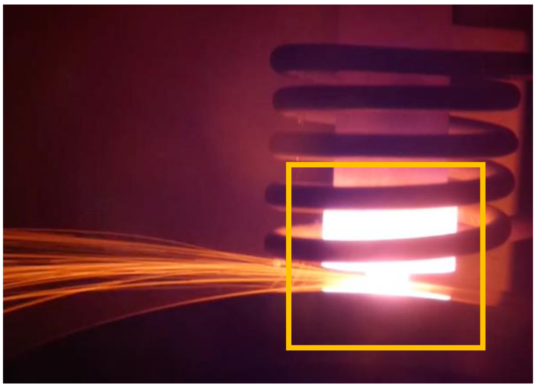

(a)

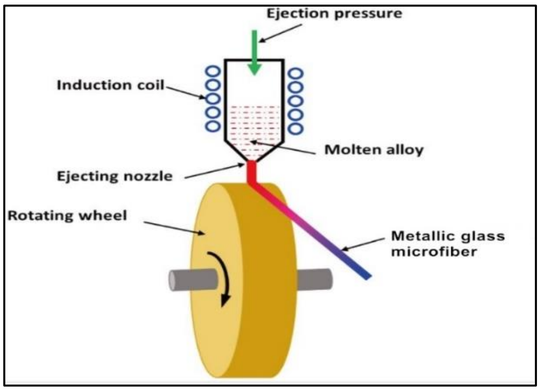

(b)

(c)

(d)

Figure 2.1 (a) Melt-Spinning process of metallic glass microfibers. (b) Basic configuration of a single-roller melt-spinning apparatus. (c) The metallic glass microfibers treated by melt spinning process. (d) The general dimension of the metallic glass microfibers.

Table 2.1 The properties of the prepared samples and new names.

New name	**Chemical Composition**	**Density [g/cm^3]**	**Melting point [°C]**
MM1	$Fe_{80}Si_5B_{15}$	7.2	1168.5
MM2	$Fe_{80}Si_5B_{15}$	7.2	1168.5
MM3	$Fe_{72}B_{19}Si_5Nb_4$	7.0	1260
MM4	$Fe_{40}Ni_{40}B_{20}$	8.4	1150
MM5	$Fe_{40}Ni_{40}B_{20}$	8.4	1150

2.2 Sintering sample preparation

Microfibers were cut into pieces and were assembled homogeneously into the square sheets with the dimension of 1.5 cm x 1.5 cm in order to go through the subsequent sintering. It is important to note that it was necessary to minimize the gaps between the microfibers to obtain more homogeneous and denser sheet during sintering. The sintered samples were further analyzed for their crystalline phases using XRD.

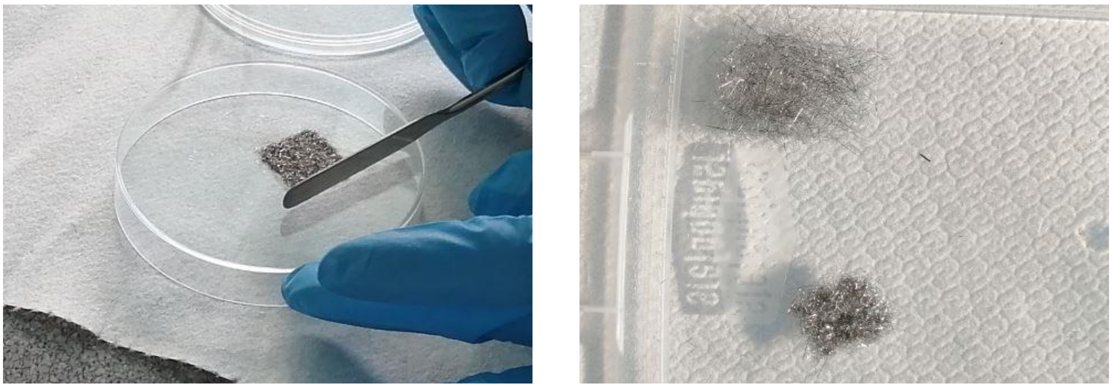

(a) **(b)**

Figure 2.2 (a) The square sheet preparation. (b) The samples before sintering and the samples after sintering.

2.3 Sample thermal treatment

The square sheets were sintered in the temperature range of 25 – 800 ℃ (Nabertherm GmbH). These sheets first were heated at a heating rate of 20 ℃/min to 800 ℃ and kept for 2 hours at 800℃, following by the furnace cooling in vacuum. During sintering, pure titanium sponge was placed next to the samples to prevent possible oxidation.

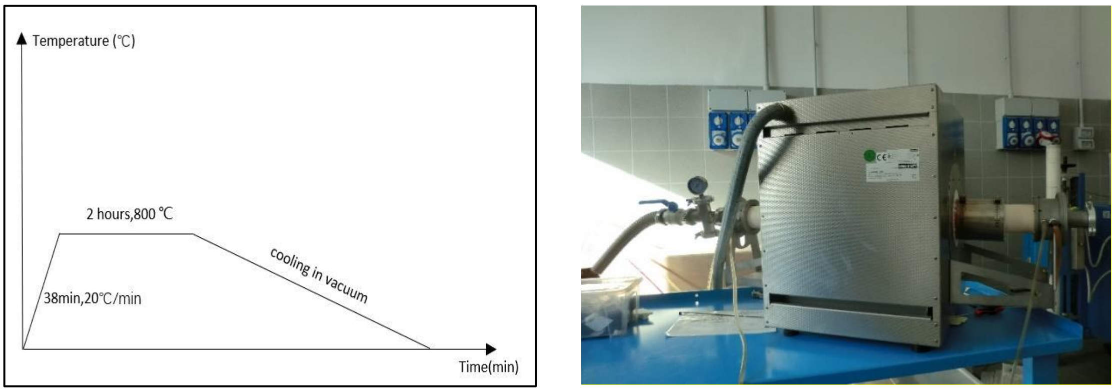

(a) **(b)**

Figure 2.3 (a) The required experimental procedures, the temperature and time of sintering. (b) The sintering furnace used in the experiment.

2.4 Crystallography and phase analysis

The microstructure of the specimens was examined by Scanning Electron Microscopy (SEM, JCM-6000Plus BENCHTOP). Further confirmation of the amorphous microstructure was realized by X-ray diffractometer (XRD, PANalytical X’Pert PRO) with Cu-Ka (l¼ 1.5418 Å) as a radiation at 40 kV and 20 mA. The studied alloys were defined as amorphous if the diffraction pattern presented the typical liquid-like structure, characteristic of an amorphous phase.

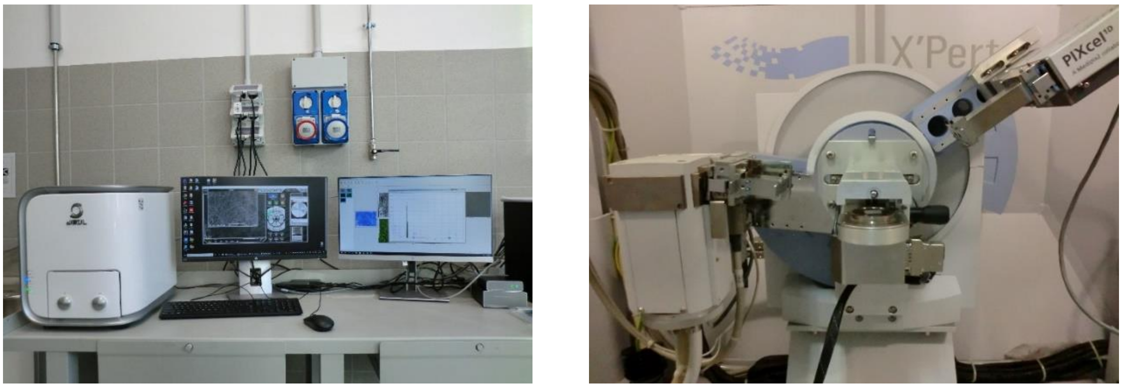

(a) **(b)**

Figure 2.4 (a) Scanning Electron Microscopy used in the experiment. (b) X-ray diffractometer used in the experiment.

2.5 Thermal properties

The thermal stability associated with glass transition (T_g) and crystallization (T_x) behavior of the studied alloys was evaluated by differential scanning calorimetry (DSC, NETZSCH DSC404 F3) at a continuous heating rate of 20 K/min. The DSC tests were carried out in the temperature range of 20℃– 1000℃. The sample was put into the crucible and covered, and it must be guaranteed that the outside of the crucible was clean and free of microfibers before starting the measurement. The crucible used in the experiment was made of aluminum oxide because of its high thermal conductivity and good ultra-high temperature stability. In order to ensure the reliability of the experimental data, the temperature calibration was performed with alumina powder of the same mass as the tested microfibers during the actual calorimetric examinations. Moreover, about 0.67 ml/s flow of the same highly pure argon gas was adopted in order to provide the sample protection during the measurement.

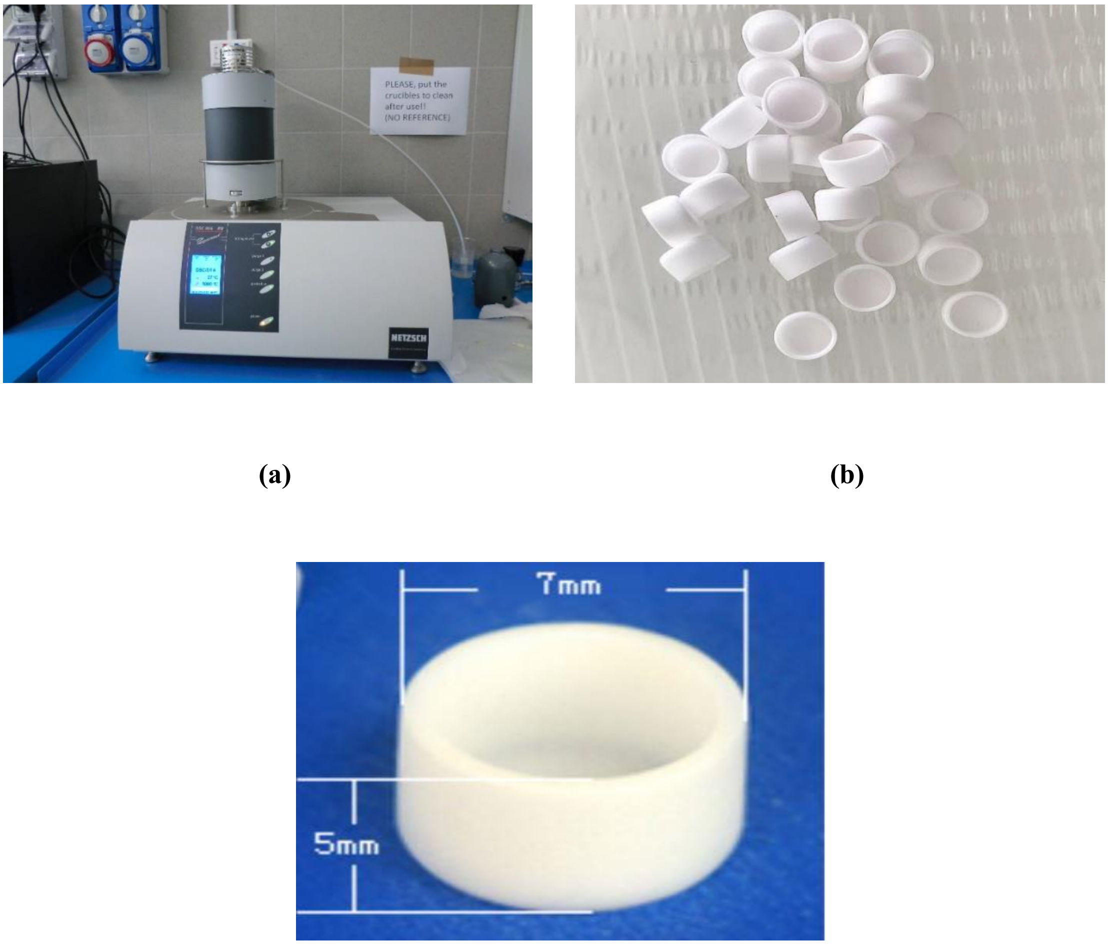

(a) **(b)**

(c)

Figure 2.5 (a) The differential scanning calorimetry used in the experiment. (b) The aluminum oxide crucible used in the experiment. (c) The dimension of the aluminum oxide crucible used in the experiment.

3. Results and discussion

3.1 Microstructure analysis

3.1.1 Starting microfibers

The microfiber samples used in this study are presented in Figure 3.1. The composition of each sample has previously introduced in Table 2.1 in the Materials and methods section. It is evident that some of the samples such as MM3 have coarser appearance in comparison with MM4 and MM5. Samples were further characterized by scanning electron microscopy (SEM) and they are shows in Figure 3.2 and Figure 3.3.

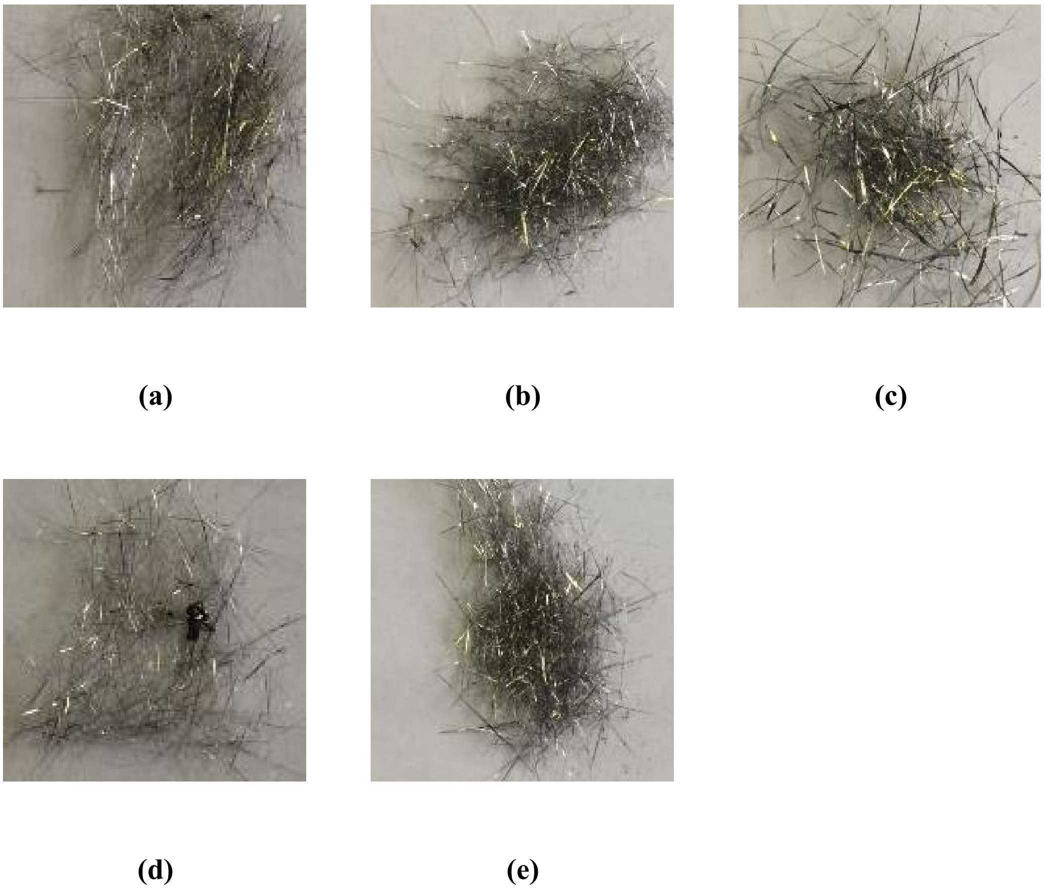

(a) **(b)** **(c)**

(d) **(e)**

Figure 3.1 Optical pictures of as-cast microfibers (a) MM1 (b) MM2 (c) MM3 (d) MM4 (e) MM5

What is clear from SEM images (Figure 3.2) is the rectangular shape of microfibers cross-sections. This could be related to the fabrication technique (modified melt-spinning technique) which was originally designed for fabrication of amorphous metallic ribbons. Controlling the surface tension of metallic melts and the experimental parameters of melt-spinning, microfibers were fabricated. Sample MM3 exhibit lots of surface defect and appears to have higher surface roughness compared to the other samples. Figure 3.3 shows the same SEM images of these samples with higher magnifications. Among them, the samples MM4 and MM5 show a relatively uniform thickness, with an average thickness of about 15μm, and the finer strip-like structures are in the majority in the displayed microstructure. The samples MM1 and MM2 also show a relatively uniform thickness, but the average thickness is about 20μm, and the microstructure is dominated by a thicker strip structure. By comparing the above four different samples, the size distribution of the samples MM4 and MM5 is more uniform and denser, with fewer voids per unit area. In addition, it is clear that the SEM images of samples MM4 and MM5 are brighter than samples MM1 and MM2. The reason may be connected to the compositional differences of MM4 and MM5 contains with the other two samples because they contain nickel which has a higher atomic number compared to silicon. Because the higher the atomic number of the substance, the brighter the image in scanning electron microscopy. Finally, the sample MM3 shows a very non-uniform thickness, with a size range of 50-300 μm. Due to the larger size, the microstructure of the sample MM3 is more flake-like and has a rough surface. According to these figures, all samples have relatively rough surfaces. By comparing the surface roughness of different samples, the sample MM4 has a smoother surface and relatively flat microstructure edges. On the contrary, the sample MM5 has a very rough surface and irregular microstructure edges, and the sample MM5 has a large number of surface defects. This could be due to hole nucleation and rotating copper wheel surface roughness during the fabrication process. Furthermore, the samples of MM1 and MM2 have smoother surfaces and flat microstructure edges, but their surfaces have a small amount of point protrusions. Finally, apart from a few surface defects and holes and point protrusions, the surface of the sample MM3 also has ring-shaped markings.

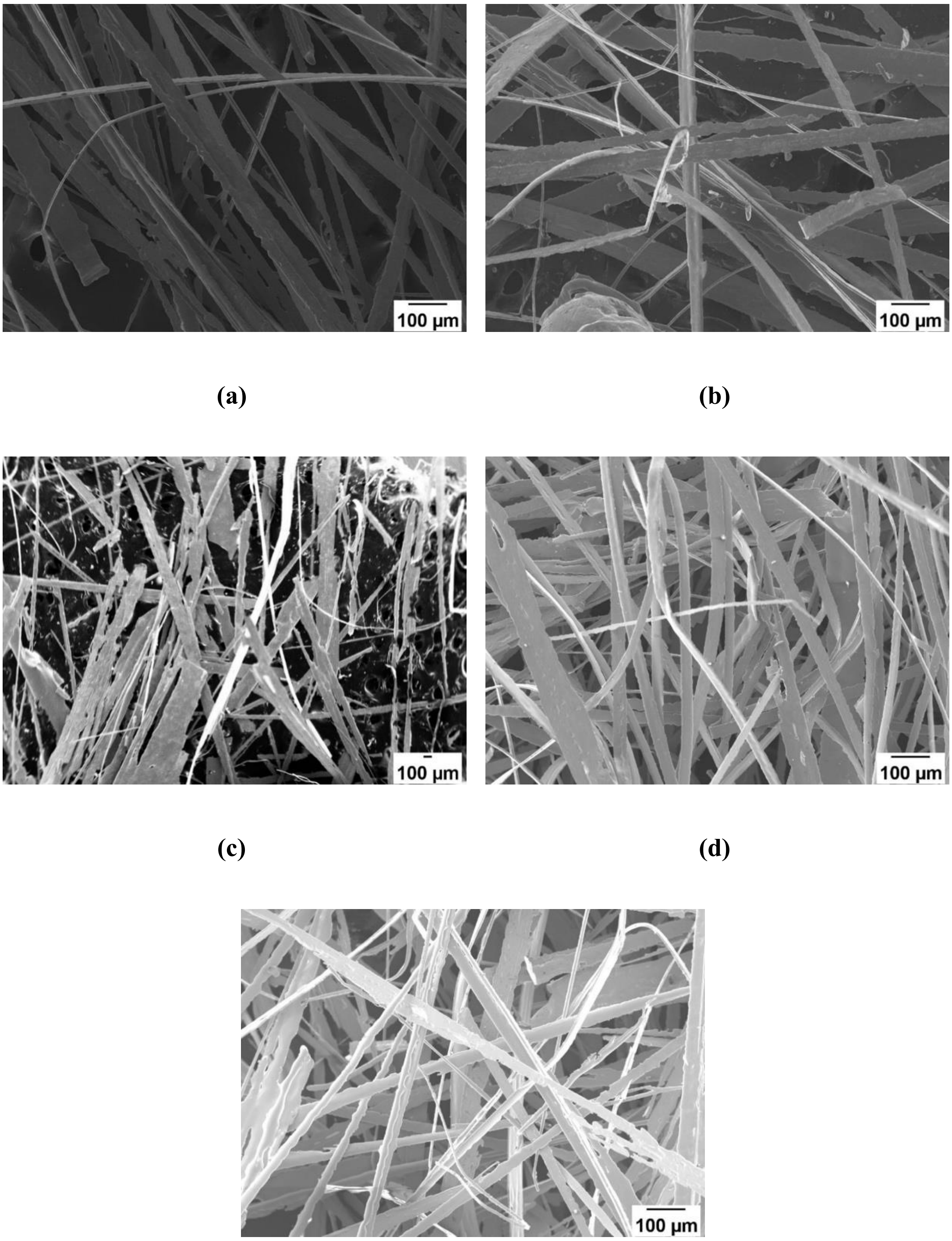

(a) **(b)**

(c) **(d)**

(e)

Figure 3.2 Scanning electron microscopy of samples (a) MM1 (b) MM2 (c) MM3 (d) MM4 (e) MM5

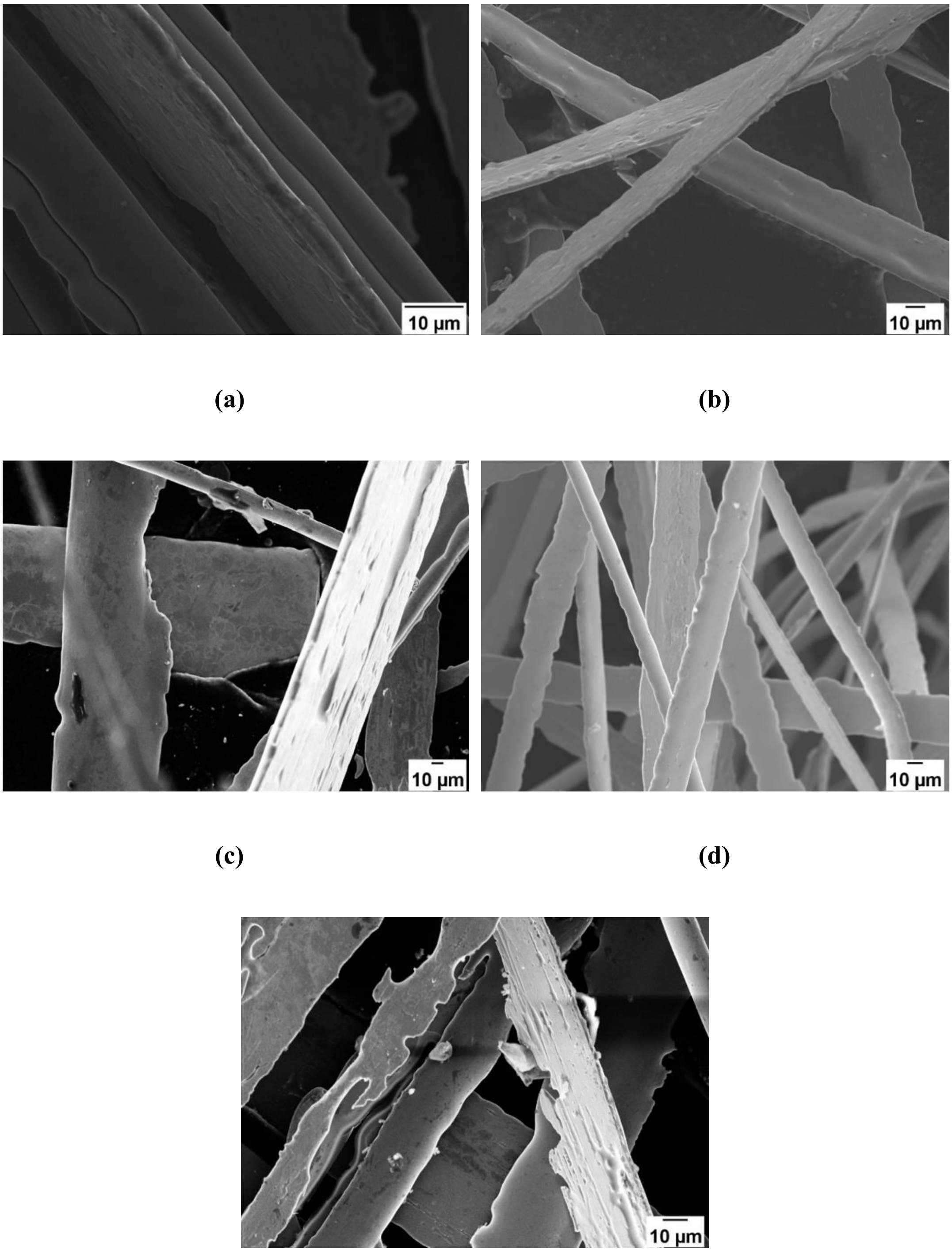

(a) **(b)**

(c) **(d)**

(e)

Figure 3.3. Higher magnification scanning electron microscopy of samples (a) MM1 (b) MM2 (c) MM3 (d) MM4 (e) MM5

3.1.2 Sintered samples

Sintering experiments were conducted as described before in the section 2.3 (Sample thermal treatment). Figure 3.4 shows the optical images of microfibers after the sintering process. In this experiment, the author separately performed sintering treatment, under the same conditions, on the iron-based metallic glass samples involved in this paper. Due to the different physical characteristics of different iron-based metallic glass samples, the sintered sample of MM2 iron-based metallic glass materials did not show expected result. There are numbers of reasons that could lead to this result among which are the microfiber dimensions which are coarser in MM2 compared to MM1 with the exact same composition. The other speculation is the thickness of the prepared sheet was too high to effectively gets interconnected. Various of temperature and other sources of errors related to the experiment is another possibility. Going back to Figure 3.4, other samples (MM1, MM3, MM4, and MM5) show successful sintered products. Among them, the sintered samples of MM1, MM3 and MM4 are better interconnected to form a sheet. This is important because it will eventually affect the mechanical strength and the density of the prepared sheet. As far as the oxidation reaction is concerned, the surface of the sintered sample MM1 is darker and there is less light reflection, which indicates that the MM1 sample is possibly partially oxidized during the sintering process.

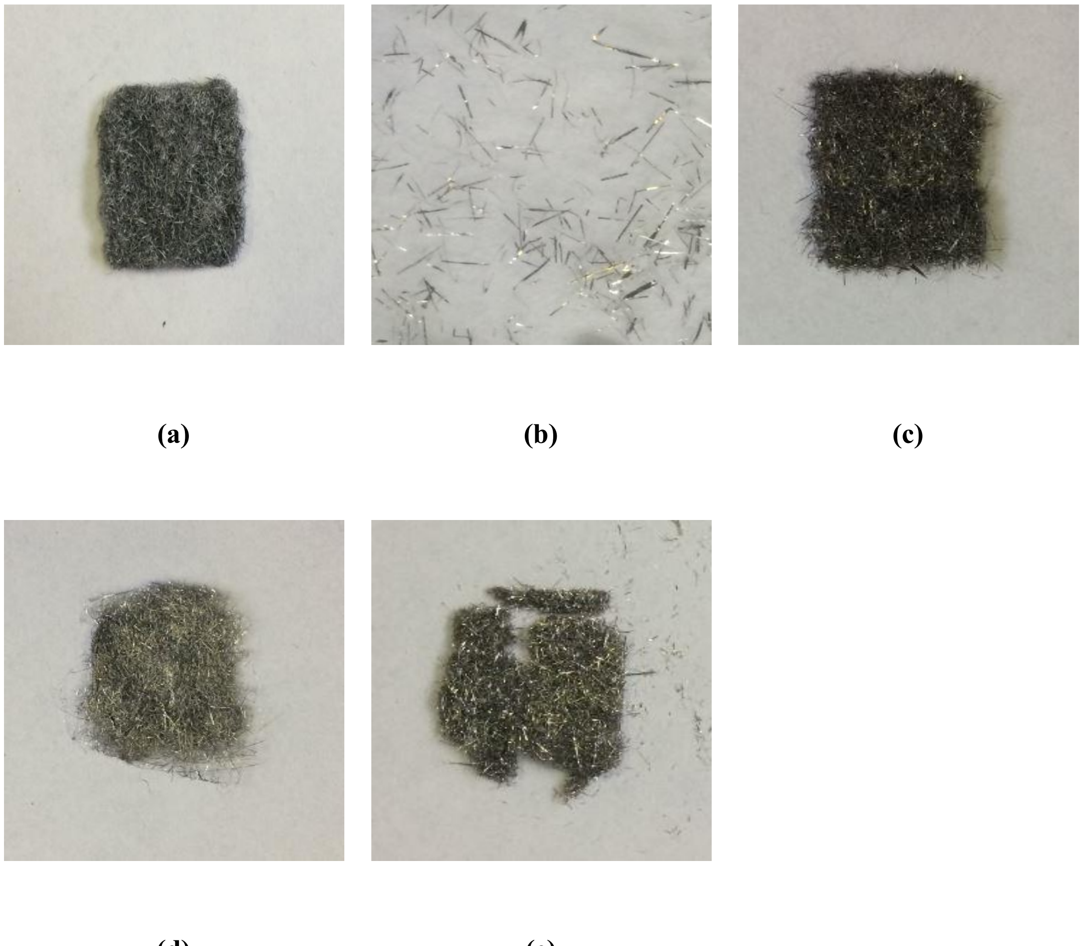

Figure 3.4. Optical picture of samples after sintering (a) MM1 (b) MM2 (c) MM3 (d) MM4 (e) MM5

3.2 Thermal analysis: differential scanning calorimetry (DSC)

3.2.1 Thermal stability of the metallic glasses

Some available data from the DSC patterns recorded at a heating rate of 20 K/min (temperatures in °C) is listed in Table 3.1. According to the Table 3.1， T_g stands for the glass transition temperature measured at the onset of the transformation, T_{xi} (i = 1 to 2) for the onset temperature of the i crystallization event, T_{ci} (i = 1 to 2) for the temperature of the peak. Peak area is the difference of specific heat at the crystallization zone, ΔT is the supercooled liquid region and ΔT_x is the difference of temperature between different peaks.

DSC analysis for samples with the chemical composition of $Fe_{80}Si_5B_{15}$ (MM1 and MM2) are shown in Figure 3.5 and Figure 3.6. According to these figures, both MM1 and MM2 present similar thermal behavior, showing two exothermic peaks at temperature range between 480°C- 540°C, and the temperature corresponding to two crystallization processes that initiation of each step is distinguished by T_{x1}–T_{x2} on the DSC curve. The first one is characterized by a relatively smaller peak, associated with the crystallization of the amorphous matrix. In contrast, the second peak which is sharper, might be induced by the secondary crystallization of the remaining amorphous phase or the transformation of the primary metastable phase. The T_{x1} and T_{c1} of MM1 occur at 496°C and 506°C which are shifted to higher temperatures for MM2 at 501°C and 511°C respectively. Similar trend is observed for the second exothermic peak where T_{x2} and T_{c2} of MM1 occur at 521°C and 531°C respectively and these temperatures are slightly shifted for MM2 to higher temperature at 526°C and 536°C. However, the main difference between MM1 and MM2 is the area under their peaks. The measured area for MM1 (86 μV•°C/mg) is more than two times larger than MM2 (35 μV•°C/mg). This might be related to the cooling rate they went through during the fabrication by melt-spinning. Higher cooling rate result in larger exothermic peaks. The other difference is their glass transition temperature. MM1 shows T_g at 426°C while T_g for MM2 is shifted to higher temperature, 456°C.

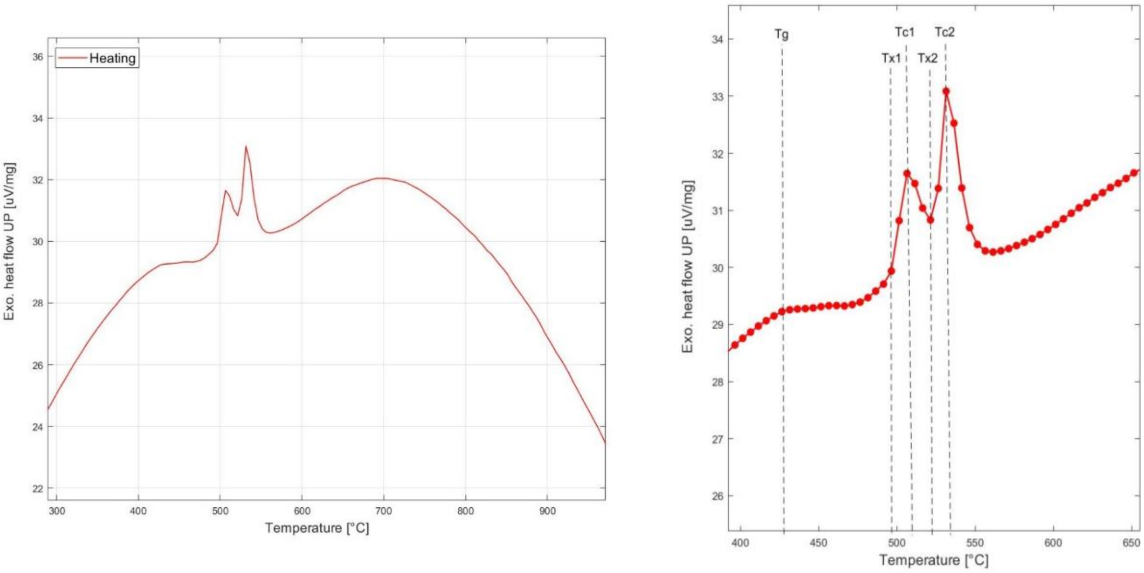

(a) **(b)**

Figure 3.5 (a) DSC curve of the MM1 performed at a heating rate of 20 K/min. (b) The local enlargement of the curve MM1 evidencing the glass transition.

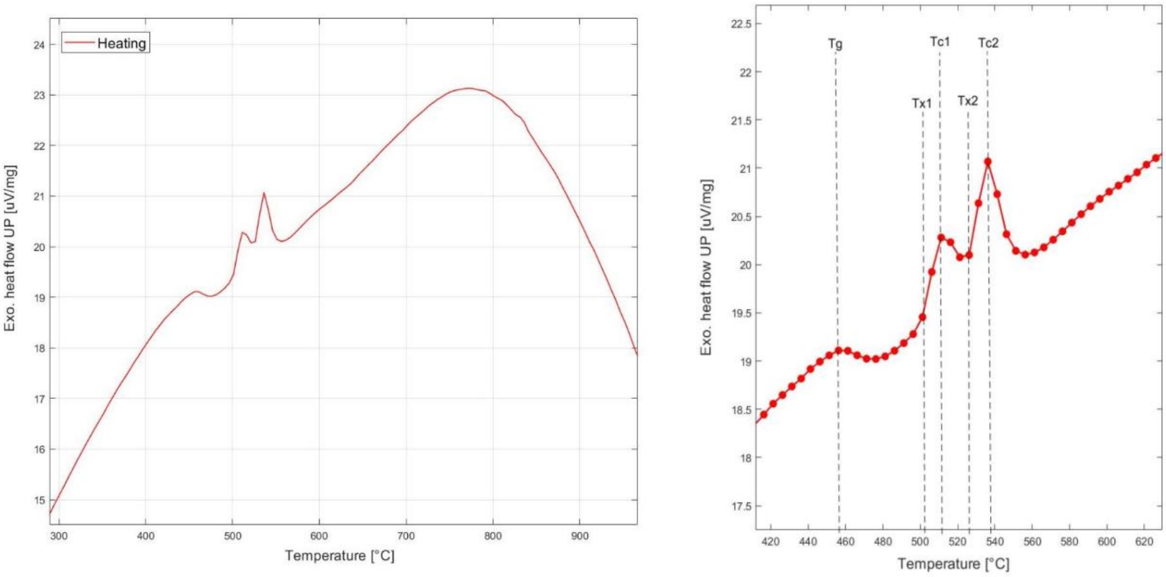

(a) **(b)**

Figure 3.6 (a) DSC curve of the MM2 performed at a heating rate of 20 K/min. (b) The local enlargement of the curve MM2 evidencing the glass transition.

DSC analysis of MM3 is not presented in this section due to technical problems associated with the DSC device. Moving on to the $Fe_{40}Ni_{40}B_{20}$ composition (MM4 and MM5), their DSC analysis are shown in Figure 3.7 and Figure 3.8. Unlike MM1 and MM2, these samples show only one exothermic peak indicating only one crystallization event. The initiation of crystallization is marked as T_{x1} on DSC curve. The measured T_{x1} and T_{c1} for MM4 are at 401°C and 421°C which are almost the same, slightly shifted to higher temperatures, for MM5 at 405°C and 424°C. Their glass transition temperature is found at an identical temperature 376˚C. Furthermore, the peak area of sample MM5 (167 µV•°C/mg) is much larger than that of sample MM4 (44 µV•°C/mg), which indicates the heat released per unit weight of the sample MM5 is relatively high. This is due to the higher cooling rate MM5 samples went through compared to MM4. In fact, the wheel velocity during melt-spinning was set at 63 m/s for MM5 while it was set at 51 m/s for MM4.

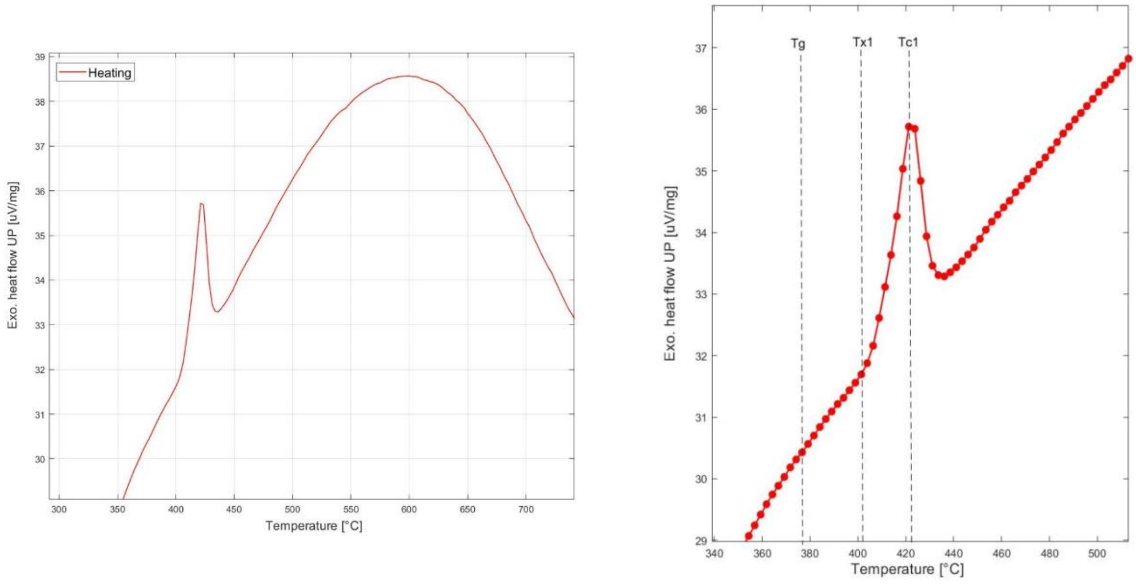

(a) **(b)**

Figure 3.7 (a) DSC curve of the MM4 performed at a heating rate of 20 K/min. (b) The local enlargement of the curve MM4 evidencing the glass transition.

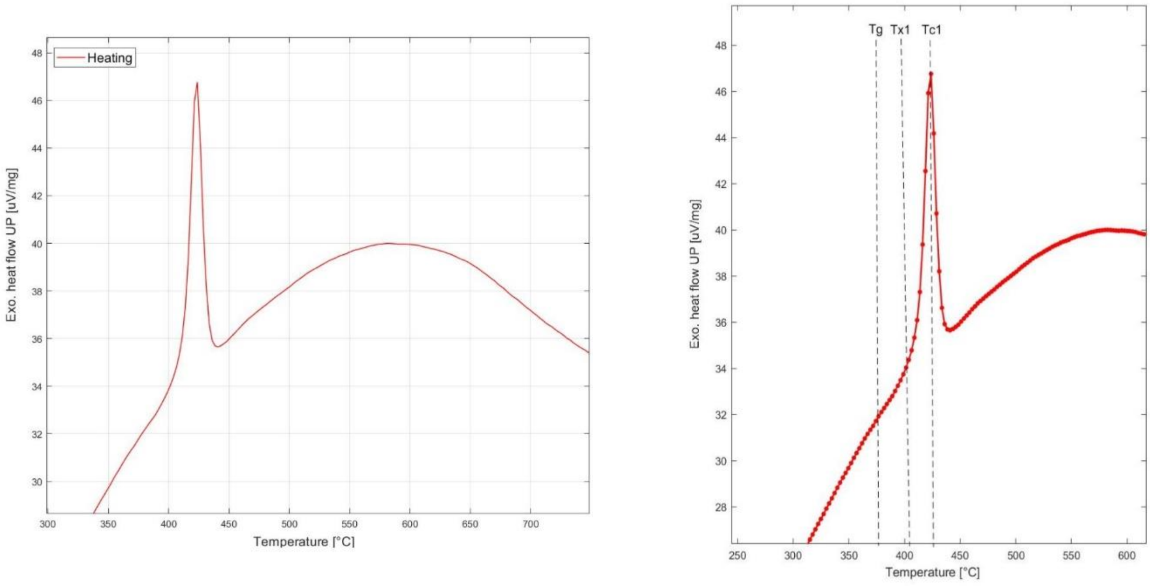

(a) **(b)**

Figure 3.8 (a) DSC curve of the MM5 performed at a heating rate of 20 K/min. (b) The local enlargement of the curve MM5 evidencing the glass transition.

The summary of the most important information extracted from these DSC curves is presented at Table 3.1. According to this table, sample MM2 has outstanding thermal stability and heat resistance, and the sample MM5 releases the most heat during the crystallization process. Larger $\Delta T = T_{x1} - T_g$ for $Fe_{80}Si_5B_{15}$ samples compared to $Fe_{40}Ni_{40}B_{20}$ samples shows once again that the introduction of Si is an effective way to enhance the thermal stability of the supercooled liquid [147].

Table 3.1. Data from the DSC patterns recorded at a heating rate of 20 K/min (temperatures in °C).

Sample/ Analysis	Unit	MM1	MM2	MM4	MM5
Tg	[°C]	426.4	456.2	376.7	376.8
Tx1	[°C]	496.4	501.2	401.4	404.5
Tc1	[°C]	506.4	511.2	421.3	423.9
Tx2	[°C]	521.4	526.2	-	-
Tc2	[°C]	531.4	536.2	-	-

Peak area	[µV•°C/mg]	86.23	34.59	44.14	166.79
ΔT=Tx1-Tg	[°C]	70	45	24.7	19.4
ΔTx=Tx2-Tx1	[°C]	25	25	-	-

3.3 XRD analysis

The XRD analysis of as-cast samples are presented in Figure 3.9. The pattern consists of a broad diffused maximum without diffraction peaks which indicates the amorphous phase for all the sample. This means that the cooling rate used to fabricate these samples was higher than the critical cooling rate required to suppress any crystallization event. Indeed, the critical cooling rate for glass formation, Rc, is an important characteristic parameter for predicting the ease or difficulty of glass formability. It is defined as the minimum cooling rate necessary to keep the melt amorphous without detectable crystallization upon solidification. A slower Rc indicates a greater glass-forming ability of an alloy system.

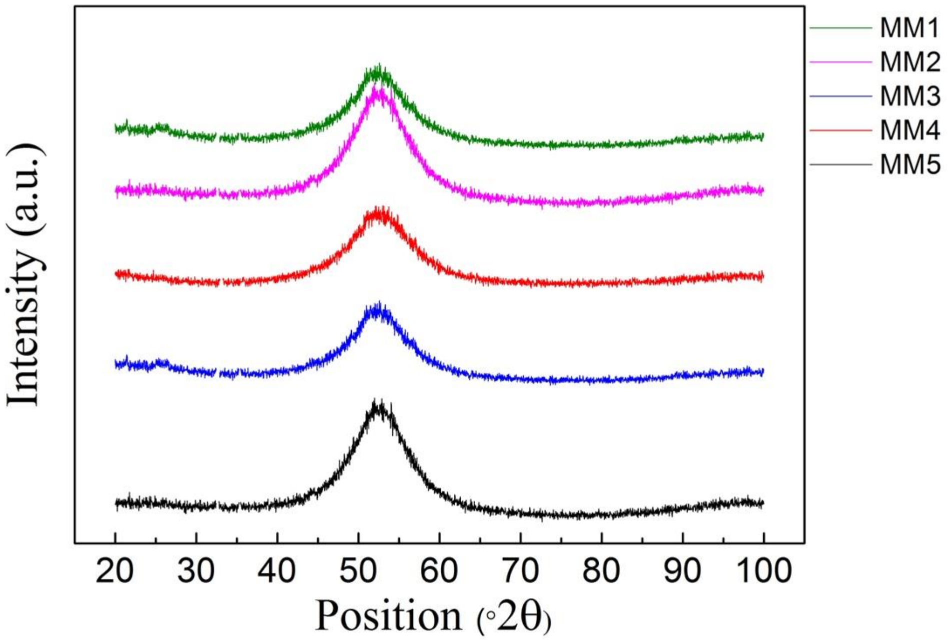

Figure 3.9 The XRD results for as-cast metallic microfibers MM1, MM2, MM3, MM4, and MM5.

Moving on to the XRD analysis after sintering, Figure 3.10 shows X-ray diffraction patterns of all the samples after sintering. The XRD pattern shows a superposition of a broad diffuse background and a set of diffracted peaks which implies that partly amorphous-crystalline composite obtained after sintering. And in fact, the amorphous phase is still present in the samples.

Starting with sample MM1, the phases formed which are identified after sintering are Fe_3Si, FeSi. The number of identified crystal phases corresponds to the number of peaks expressed in the previous DSC curve. Among the phases formed, Fe_3Si is an important magnetic functional material with high temperature resistance, corrosion resistance, oxidation resistance, low conductivity and excellent soft magnetic ability, moreover, Fe_3Si also has a negative temperature coefficient. Expecting to see similar crystalline phases for MM2 (due to the same chemical composition), the crystalline phases in MM2 are identified to be Fe_3Si, Fe. This is in line with our previous observation for MM2 DSC analysis. The presence of two exothermic peaks indicated two crystallization events which should be related to these two crystallize phases, Fe_3Si and Fe. According to previously reported data, the first exothermic peak at MM2 DSC curve should corresponds to the formation of the Fe_3Si phase [149–152]. while the second one corresponds to the formation of the Fe, because we only found two crystalline phases in the XRD analysis of the sintered sample MM2. It can be concluded that for the sintered sample MM2, the crystallization temperature of the Fe_3Si phase is 511.2°C while the crystallization temperature of the Fe is 536.2°C.

Unfortunately, the DSC analysis for MM3 was not available but the XRD analysis for MM3 indicates the presence of two crystalline phases: Fe_3Si and Fe_2B. Previously, Y.R. Zhang and R.V. Ramanujan have reported similar observation for compositions similar to $Fe_{80}Si_5B_{15}$ alloy [148]. Compared to MM2 with the composition of $Fe_{80}Si_5B_{15}$, the XRD data suggests that the addition of Nb acts as a glue to promotes the formation of Fe_2B phase. Here, with the addition of 4 at.% Nb, the crystallization mechanism might have been changed from primary crystallization to eutectic crystallization.

Nevertheless, Samples MM4 and MM5 both only identify one different crystalline phase. This XRD analysis result corresponds to the number of peaks shown in the previous DSC curves of samples MM4 and MM5. Furthermore, the crystals which are identified in the sintered sample MM4 is (Fe, Ni) while the phases formed in the sintered sample MM5 is Ni_3Fe. Obviously, the Ni_3Fe is the face-centered cubic structure based on a long-range ordered characteristic. The face-centered position of the face-centered cubic unit cell is occupied by Ni atoms, and the top corner positions are occupied by Fe atoms. What is more, the Ni_3Fe also exhibits typical ferromagnetism at room temperature. Finally, the same composition of sample MM4 and sample MM5 form the different crystalline phases. The hypothetical reasons are 1. The sample underwent various degrees of oxidation during the sintering process. 2. The sample MM5 had a higher cooling rate when making the starting microfibers.

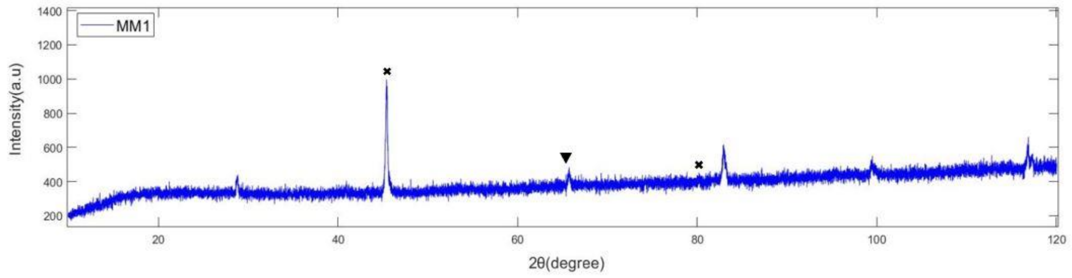
MM1
Intensity(a.u)
2θ(degree)
1400
1200
1000
800
600
400
200
20
40
60
80
100
120

(a)

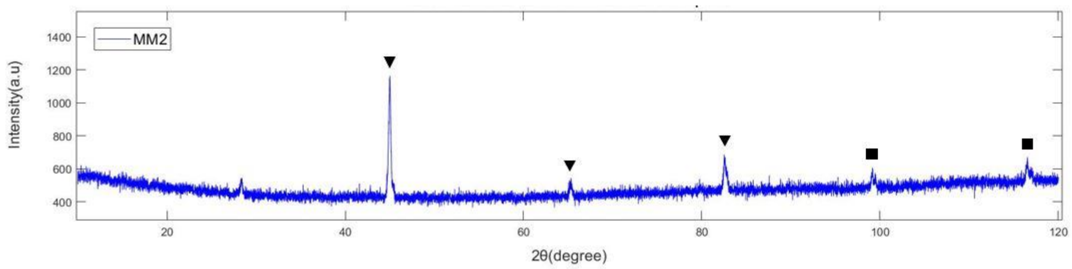
MM2
Intensity(a.u)
2θ(degree)
1400
1200
1000
800
600
400
20
40
60
80
100
120

(b)

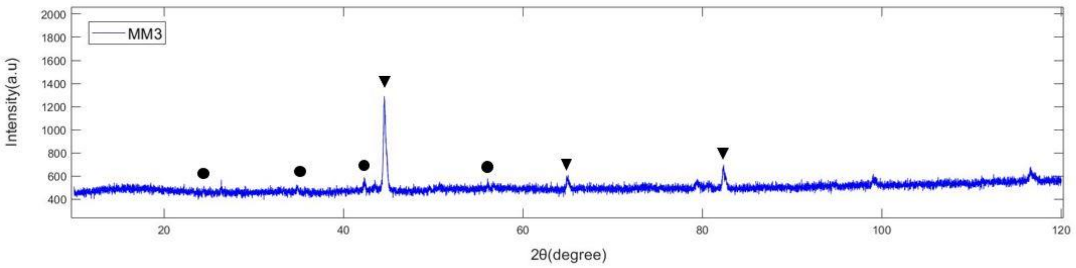
MM3
Intensity(a.u)
2θ(degree)
2000
1800
1600
1400
1200
1000
800
600
400
20
40
60
80
100
120

(c)

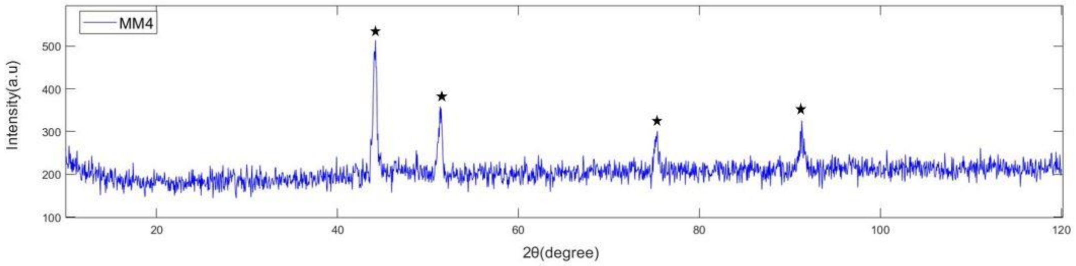
MM4
Intensity(a.u)
2θ(degree)
500
400
300
200
100
20
40
60
80
100
120

(d)

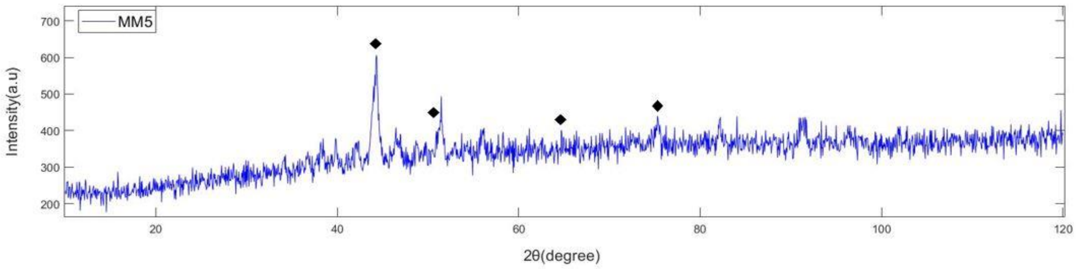

(e)

Figure 3.10 XRD results for the samples after sintering: (a) MM1 (b) MM2 (c) MM3 (d) MM4 (e) MM5: Fe_3Si(▼) FeSi(X) Fe(■) Fe_2B(●) [Fe , Ni](★) Ni_3Fe(◆)

The summary of important information from the XRD data analysis are presented for each sample from Table 3.2 to Table 3.6.

Table 3.2 The XRD scan parameters of the sintered sample MM1.

Pos. of peak	**Height**	**FWHM**	**d-spacing**	**Rel. Int.**	**Tip width**	**Chem. Formula**
[°2Th.]	**[cts]**	**[°2Th.]**	**[Å]**	**[%]**	**[°2Th.]**	**-**
45.4006	604.94	0.1008	1.99606	100	0.121	FeSi
65.8443	164.95	0.001	1.4173	27.27	0.0012	Fe_3Si
80.2947	117.79	0.0231	1.19471	19.47	0.0278	FeSi

Table 3.3 The XRD scan parameters of the sintered sample MM2.

Pos. of peak	**Height**	**FWHM**	**d-spacing**	**Rel. Int.**	**Tip width**	**Chem. Formula**
[°2Th.]	**[cts]**	**[°2Th.]**	**[Å]**	**[%]**	**[°2Th.]**	**-**
44.9967	724.89	0.1378	2.0147	100	0.1653	Fe_3Si
65.32	90.91	0.1929	1.42858	12.54	0.2314	Fe_3Si
82.6239	177.4	0.1929	1.16781	24.47	0.2314	Fe_3Si
99.1695	95.67	0.1008	1.01173	13.2	0.121	Fe
99.4877	54.68	0.1653	1.01019	7.54	0.1984	Fe
116.5444	125.35	0.1344	0.90564	17.29	0.1613	Fe
116.9821	59.67	0.2016	0.90351	8.23	0.2419	Fe

Table 3.4 The XRD scan parameters of the sintered sample MM3.

Pos. of peak	**Height**	**FWHM**	**d-spacing**	**Rel. Int.**	**Tip width**	**Chem. Formula**
[°2Th.]	**[cts]**	**[°2Th.]**	**[Å]**	**[%]**	**[°2Th.]**	**-**
24.4672	24.98	0.1929	3.63825	3.41	0.2314	Fe_2B
34.8653	46.64	0.1653	2.57335	6.38	0.1984	Fe_2B
42.3507	92.22	0.1102	2.13424	12.61	0.1322	Fe_2B
44.5234	731.56	0.0551	2.03501	100	0.0661	Fe_3Si
56.1042	40.69	0.2204	1.63933	5.56	0.2645	Fe_2B

65.0212	98.37	0.1653	1.43442	13.45	0.1984	Fe_3Si
82.3564	181.03	0.168	1.16995	24.75	0.2016	Fe_3Si

Table 3.5 The XRD scan parameters of the sintered sample MM4.

Pos. of peak	**Height**	**FWHM**	**d-spacing**	**Rel. Int.**	**Tip width**	**Chem. Formula**
[°2Th.]	**[cts]**	**[°2Th.]**	**[Å]**	**[%]**	**[°2Th.]**	**-**
44.2607	255.37	0.3651	2.04647	100	0.4381	(Fe , Ni)
51.416	126.15	0.3129	1.77723	49.4	0.3755	(Fe , Ni)
75.5823	113.72	0.8872	1.25809	44.53	1.0646	(Fe , Ni)
91.343	123.75	0.3816	1.07682	48.46	0.4579	(Fe , Ni)

Table 3.6 The XRD scan parameters of the sintered sample MM5.

Pos. of peak	**Height**	**FWHM**	**d-spacing**	**Rel. Int.**	**Tip width**	**Chem. Formula**
[°2Th.]	**[cts]**	**[°2Th.]**	**[Å]**	**[%]**	**[°2Th.]**	**-**
44.3528	287.43	0.2086	2.04244	100	0.2503	Ni_3Fe
51.4131	108.99	0.4172	1.77733	37.92	0.5007	Ni_3Fe
64.7007	123.88	0.3798	1.44075	43.1	0.4558	Ni_3Fe
75.416	62.27	0.4172	1.26045	21.66	0.5007	Ni_3Fe

4. Conclusions

In this work, amorphous metal microfibers with three different compositions, $Fe_{80}Si_5B_{15}$, $Fe_{72}Si_5B_{19}Nb_4$, and $Fe_{40}Ni_{40}B_{20}$, were characterized and sintered at elevated temperatures. Their microstructure, phase analysis and thermal properties were investigated before and after sintering. DSC, XRD, and SEM were used as the investigation techniques in this work. Combining the results obtained, the following conclusions can be drawn:

1. The samples MM1 and MM2 show a relatively uniform thickness, but the average thickness is about 20μm, and the microstructure is dominated by a thicker strip structure while the samples MM4 and MM5 show an average thickness of about 15μm, and the finer strip-like structures are in the majority in the displayed microstructure. Finally, the sample MM3 shows a very non-uniform thickness, with a size range of 50-300μm.

2. Regarding the sintering results, MM1 shows traces of partial oxidation on its surface after sintering while MM2 fails to be interconnected after sintering.

3. Both MM1 and MM2 present similar thermal behavior, showing two exothermic peaks. In contrast, MM4 and MM5 show only one exothermic peak indicating only one crystallization event. The glass transition temperatures for the studied samples are T_g=426°C for MM1, T_g=456°C for MM2 and T_g= 376°C for both MM4 and MM5. Due to the measured area for MM1 is larger than that for MM2, it can be concluded that the cooling rate of MM1 is higher than that for MM2. Similarly, the cooling rate of MM5 is higher than that for MM4. Finally, sample MM2 has outstanding thermal stability and heat resistance, and the sample MM5 releases the most heat during the crystallization process. Larger $\Delta T=T_{x1}-T_g$ for $Fe_{80}Si_5B_{15}$ samples compared to $Fe_{40}Ni_{40}B_{20}$ samples shows once again that the introduction of Si is an effective way to enhance the thermal stability of the supercooled liquid.

4. The phases formed which are identified in MM1 are Fe_3Si, FeSi. The crystalline phases in MM2 are identified to be Fe_3Si, Fe. It can be concluded that for the sintered MM2, the crystallization temperature of the Fe_3Si phase is 511°C while the crystallization temperature of the Fe is 536°C. The XRD analysis for MM3 indicates the presence of two crystalline phases: Fe_3Si and Fe_2B. Nevertheless, Samples MM4 and MM5 both only identify one different crystalline phase. The crystals which are identified in the sintered MM4 is (Fe, Ni) while the phases formed in the sintered MM5 is Ni_3Fe.

Abbreviations

AC	lternating current
AFM	Atomic force microscopy
BMG	Bulk metallic glasses
DC	Direct current
DSC	Differential scanning calorimetry
DMLS	Direct Metal Laser Sintering process
EIS	Electrochemical impedance spectroscopy
GFA	Glass forming ability
LPHS	Liquid phase separation
MG	Metallic glasses
RE	Rare earth
SEM	Scanning Electron Microscopy
STZ	Shear transformation zone
TTZ	Tension transformation zone
XRD	X-ray diffractometry

List of Figures

Fig. 1.1 Typical DSC curves and XRD patterns for the $Fe_{73}Al_5Ga_2P_{11}C_5B_4$ rods 6

Fig. 2.1 (a) Melt-Spinning process of metallic glass microfibers. (b) Basic configuration of a single-roller melt-spinning apparatus. (c) The metallic glass microfibers treated by melt spinning process. (d) The general dimension of the metallic glass microfibers. 11

Fig. 2.2 (a) The square sheet preparation. (b) The samples before sintering and the samples after sintering........ 12

Fig. 2.3 (a) The required experimental procedures, the temperature and time of sintering. (b) The sintering furnace used in the experiment........ 13

Fig. 2.4 (a) Scanning Electron Microscopy used in the experiment. (b) X-ray diffractometer used in the experiment........ 14

Fig. 2.5 (a) The differential scanning calorimetry used in the experiment. (b) The differential thermal analysis used in the experiment. (c) The aluminum oxide crucible used in the experiment. (d) The dimension of the aluminum oxide crucible used in the experiment........ 15

Fig. 3.1 Optical pictures of as-cast microfibers 16

Fig. 3.2 Scanning electron microscopy of samples........ 18

Fig. 3.3 Higher magnification scanning electron microscopy of samples 19

Fig. 3.4 Optical picture of samples after sintering 20

Fig. 3.5 (a) DSC curve of the MM1 performed at a heating rate of 20 K/min. (b) The local enlargement of the curve MM1 evidencing the glass transition........ 22

Fig. 3.6 (a) DSC curve of the MM2 performed at a heating rate of 20 K/min. (b) The local enlargement of the curve MM2 evidencing the glass transition........ 22

Fig. 3.7 (a) DSC curve of the MM4 performed at a heating rate of 20 K/min. (b) The local enlargement of the curve MM4 evidencing the glass transition........ 23

Fig. 3.8 (a) DSC curve of the MM5 performed at a heating rate of 20 K/min. (b) The local enlargement of the curve MM5 evidencing the glass transition............................ 24

Fig. 3.9 The XRD results for the sample MM4 before sintering, The data from reference 25

Fig. 3.10 Figure 3.10 XRD results for the samples after sintering: (a) MM1 (b) MM2 (c) MM3 (d) MM4 (e) MM5 28

List of Tables

Table 2.1 The properties of the prepared samples and new names 12

Table 3.1 Data from the DSC patterns recorded at a heating rate of 20 K/min 24

Table 3.2 The XRD scan parameters of the sintered sample MM1 28

Table 3.3 The XRD scan parameters of the sintered sample MM2 29

Table 3.4 The XRD scan parameters of the sintered sample MM3 29

Table 3.5 The XRD scan parameters of the sintered sample MM4 30

Table 3.6 The XRD scan parameters of the sintered sample MM5 30

References

[1] Chen M. Mechanical behavior of metallic glasses: microscopic understanding of strength and ductility. Annu Rev Mater Res 2008;38:44569.

[2] Inoue A, Takeuchi A. Recent development and application products of bulk glassy alloys. Acta Mater 2011;59:2243–67.

[3] Johnson WL. Bulk glass-forming metallic alloys: science and technology. MRS Bull 1999;24:42–56.

[4] Schuh CA, Hufnagel TC, Ramamurty U. Mechanical behavior of amorphous alloys. Acta Mater 2007;55:4067–109.

[5] Trexler MM, Thadhani NN. Mechanical properties of bulk metallic glasses. Prog Mater Sci 2010;55:759–839.

[6] Klement W, Willens RH, Duwez P. Non-crystalline structure in solidified gold–silicon alloys. Nature 1960;187:869–70.

[7] Inoue A, Zhang T, Masumoto T. Zr-Al-Ni amorphous alloys with high glass transition temperature and significant supercooled liquid region. Mater Trans, JIM 1990;31:177–83.

[8] Inoue A, Zhang T, Nishiyama N, Ohba K, Masumoto T. Preparation of 16 mm diameter rod of amorphous Zr65Al7.5Ni10Cu17.5 alloy. Mater Trans, JIM 1993;34:1234–7.

[9] Inoue A. High strength bulk amorphous alloys with low critical cooling rates (overview). Mater Trans, JIM 1995;36:866–75.

[10] Peker A, Johnson WL. A highly processable metallic glass: Zr41.2Ti13.8Cu12.5Ni10.0Be22.5. Appl Phys Lett 1993;63:2342–4.

[11] Zhang QS, Deng YF, Zhang HF, Ding BZ, Hu ZQ. Cyclic softening of Zr55Al10Ni5Cu30 bulk amorphous alloy. J Mater Sci Lett 2003;22:17314.

[12] Zhang W, Inoue A. Formation and mechanical strength of new Cu-based bulk glassy alloys with large supercooled liquid region. Mater Trans 2004;45:1210–3.

[13] Ponnambalam V, Poon SJ, Shiflet GJ. Fe–Mn–Cr–Mo–(Y,Ln)–C–B (Ln = Lanthanides) bulk

metallic glasses as formable amorphous steel alloys. J Mater Res 2004;19:3046–52.

[14] Lu ZP, Liu CT, Thompson JR, Porter WD. Structural amorphous steels. Phys Rev Lett 2004;92:245503.

[15] Inoue A, Nishiyama N, Matsuda T. Preparation of bulk glassy Pd40Ni10Cu30P20 alloy of 40 mm in diameter by water quenching. Mater Trans, JIM 1996;37:181–4.

[16] He Y, Schwarz RB, Archuleta JI. Bulk glass formation in the Pd–Ni–P system. Appl Phys Lett 1996;69:1861–3.

[17] He Y, Dougherty GM, Shiflet GJ, Poon SJ. Unique metallic glass formability and ultra-high tensile strength in Al-Ni-Fe-Gd alloys. Acta Metall Mater 1993;41:337–43.

[18] Inoue A, Sobu S, Louzguine DV, Kimura H, Sasamori K. Ultrahigh strength Al-based amorphous alloys containing Sc. J Mater Res 2004;19:1539–43.

[19] Yi S, Park TG, Kim DH. Ni-based bulk amorphous alloys in the Ni–Ti–Zr–(Si, Sn) system. J Mater Res 2000;15:2425–30.

[20] Choi-Yim H, Xu D, Johnson WL. Ni-based bulk metallic glass formation in the Ni–Nb–Sn and Ni–Nb–Sn–X (X = B,Fe,Cu) alloy systems. Appl Phys Lett 2003;82:1030–2.

[21] Zhang T, Inoue A. New bulk glassy Ni-based alloys with high strength of 3000 MPa. Mater Trans 2002;43:708–11.

[22] Louzguine DV, Inoue A. Nanocrystallization of Cu–(Zr or Hf)–Ti metallic glasses. J Mater Res 2002;17:2112–20.

[23] Inoue A, Nakamura T, Nishiyama N, Masumoto T. Mg-Cu-Y bulk amorphous alloys with high tensile strength produced by a high-pressure die casting method. Mater Trans, JIM 1992;33:937–45.

[24] Inoue A, Masumoto T. Mg-based amorphous alloys. Mater Sci Eng, A 1993;173:1–8.

[25] Lin XH, Johnson WL. Formation of Ti–Zr–Cu–Ni bulk metallic glasses. J Appl Phys 1995;78:6514–9.

[26] He G, Eckert J, Hagiwara M. Glass-forming ability and crystallization behavior of Ti–Cu–Ni–Sn–M (M = Zr, Mo, and Ta) metallic glasses. J Appl Phys 2004;95:1816–21.

[27] Li R, Pang S, Ma C, Zhang T. Influence of similar atom substitution on glass formation in (La–Ce)–Al–Co bulk metallic glasses. Acta Mater 2007;55:3719–26.

[28] Jiang QK, Zhang GQ, Chen LY, Wu JZ, Zhang HG, Jiang JZ. Glass formability, thermal stability and mechanical properties of La-based bulk metallic glasses. J Alloy Compd 2006;424:183–6.

[29] Inoue A. Stabilization of metallic supercooled liquid and bulk amorphous alloys. Acta Mater 2000;48:279–306.

[30] Löffler JF. Bulk metallic glasses. Intermetallics 2003;11:529–40.

[31] Inoue A, Shen B, Takeuchi A. Developments and applications of bulk glassy alloys in late transition metal base system. Mater Trans, JIM 2006;47:1275–85.

[32] Peter WH, Buchanan RA, Liu CT, Liaw PK, Morrison ML, Horton JA, et al. Localized corrosion behavior of a zirconium-based bulk metallic glass relative to its crystalline state. Intermetallics 2002;10:1157–62.

[33] Morrison ML, Buchanan RA, Leon RV, Liu CT, Green BA, Liaw PK, et al. The electrochemical evaluation of a Zr-based bulk metallic glass in a phosphate-buffered saline electrolyte. J Biomed Mater Res A 2005;74A:430–8.

[34] Miller M, Liaw PK. Bulk metallic glasses: an overview. New York, NY: Springer; 2010.

[35] Inoue A, Shen B, Koshiba H, Kato H, Yavari AR. Cobalt-based bulk glassy alloy with ultrahigh strength and soft magnetic properties. Nat Mater 2003;2:661–3.

[36] Liu CT, Heatherly L, Horton JA, Easton DS, Carmichael CA, Wright JL, et al. Test environments and mechanical properties of Zr-base bulk amorphous alloys. Metall Mater Trans A 1998;29:1811–20.

[37] Donovan PE, Stobbs WM. The structure of shear bands in metallic glasses. Acta Metall 1981;29:1419–36.

[38] Pekarskaya E, Kim CP, Johnson WL. In situ transmission electron microscopy studies of shear bands in a bulk metallic glass based composite. J Mater Res 2001;16:2513–8.

[39] Li W, Bei H, Tong Y, Dmowski W, Gao YF. Structural heterogeneity induced plasticity in bulk metallic glasses: from well-relaxed fragile glass to metal-like behavior. Appl Phys Lett 2013;103:171910.

[40] Li W, Gao Y, Bei H. On the correlation between microscopic structural heterogeneity and embrittlement behavior in metallic glasses. Sci Rep 2015;5:14786.

[41] Liu YH, Wang D, Nakajima K, Zhang W, Hirata A, Nishi T, et al. Characterization of nanoscale

mechanical heterogeneity in a metallic glass by dynamic force microscopy. Phys Rev Lett 2011;106:125504.

[42] Wang G, Wang YT, Liu YH, Pan MX, Zhao DQ, Wang WH. Evolution of nanoscale morphology on fracture surface of brittle metallic glass. Appl Phys Lett 2006;89:121909.

[43] Wang G, Zhao DQ, Bai HY, Pan MX, Xia AL, Han BS, et al. Nanoscale periodic morphologies on the fracture surface of brittle metallic glasses. Phys Rev Lett 2007;98:235501.

[44] Lewandowski JJ, Shazly M, Shamimi Nouri A. Intrinsic and extrinsic toughening of metallic glasses. Scr Mater 2006;54:337–41.

[45] Lewandowski JJ, Wang WH, Greer AL. Intrinsic plasticity or brittleness of metallic glasses. Philos Mag Lett 2005;85:77–87.

[46] Spaepen F. A microscopic mechanism for steady state inhomogeneous flow in metallic glasses. Acta Metall 1977;25:407–15.

[47] Steif PS. Ductile versus brittle behavior of amorphous metals. J Mech Phys Solids 1983;31:359–88.

[48] Steif PS, Spaepen F, Hutchinson JW. Strain localization in amorphous metals. Acta Metall 1982;30:447–55.

[49] Wang Z, Wang WH. Flow unit model in metallic glasses. Acta Phys Sin 2017;66:176103.

[50] Argon AS. Plastic deformation in metallic glasses. Acta Metall 1979;27:47–58.

[51] Falk ML, Langer JS. Dynamics of viscoplastic deformation in amorphous solids. Phys Rev E 1998;57:7192–205.

[52] Langer JS. Shear-transformation-zone theory of deformation in metallic glasses. Scr Mater 2006;54:375–9.

[53] Shi Y, Falk ML. Strain localization and percolation of stable structure in amorphous solids. Phys Rev Lett 2005;95:095502.

[54] Shi Y, Falk ML. Atomic-scale simulations of strain localization in three-dimensional model amorphous solids. Phys Rev B 2006;73:214201.

[55] Jiang MQ, Ling Z, Meng JX, Dai LH. Energy dissipation in fracture of bulk metallic glasses via inherent competition between local softening and quasi-cleavage. Philos Mag 2008;88:407–26.

[56] Duwez P, Lin S. Amorphous ferromagnetic phase in iron-carbon-phosphorus alloys. J Appl Phys 1967;38:4096–7.

[57] Yamauchi K, Nakagawa Y. Amorphous ferromagnetic Fe-P-B alloys prepared by a new technique of splat cooling. Jpn J Appl Phys 1971;10:1730.

[58] Kikuchi M, Fujimori H, Obi Y, Masumoto T. New amorphous ferromagnets with low coercive force. Jpn J Appl Phys 1976;14:1077–8.

[59] Inoue A, Kobayashi K, Masumoto T. Mechanical properties and thermal stability of (Fe Co, Ni)-Mo-C quaternary amorphous alloys. Sci Rep Res Inst Tohoku Univ A 1980;28:222–30.

[60] Inoue A, Kobayashi K, Kanehira J, Masumoto T. Mechanical properties and thermal stability of (Fe Co, Ni)-MB (M = IV, V and VI group transition metals) amorphous alloys with low boron concentration. Sci Rep Res Inst Tohoku Univ A 1980;29:331–42.

[61] Datta A, DeCristofaro NJ. Magnetic amorphous metal alloys. US, 4321090; 1982.

[62] Yoshizawa Y, Oguma S, Yamauchi K. New Fe-based soft magnetic alloys composed of ultrafne grain structure. J Appl Phys 1988;64:60446.

[63] Suzuki K, Makino A, Inoue A, Masumoto T. Soft magnetic properties of nanocrystalline bcc Fe-Zr-B and Fe-M-B-Cu (M = transition metal) alloys with high saturation magnetization. J Appl Phys 1991;70:6232–7.

[64] McHenry ME, Willard MA, Laughlin DE. Amorphous and nanocrystalline materials for applications as soft magnets. Prog Mater Sci 1999;44:291–433.

[65] Schwarz R, Shen T, Harms U, Lillo T. Soft ferromagnetism in amorphous and nanocrystalline alloys. J Magn Magn Mater 2004;283:22330.

[66] Inoue A, Shinohara Y, Gook JS. Thermal and magnetic properties of bulk Fe-based glassy alloys prepared by copper mold casting. Mater Trans, JIM 1995;36:1427–33.

[67] Inoue A, Gook JS. Effect of additional elements (M) on the thermal stability of undercooled liquid in Fe72-xAl5Ga2P11C6B4Mx glassy alloys. Mater Trans, JIM 1996;37:32–8.

[68] Inoue A, Zhang T, Takeuchi A. Bulk amorphous alloys with high mechanical strength and good soft magnetic properties in Fe-TM-B (TM= IV-VIII group transition metal) system. Appl Phys Lett 1997;71:464–6.

[69] Zhang W, Inoue A. Formation and magnetic properties of bulk glassy Fe-Co-Nd-Dy-B

alloys with high boron concentrations. Mater Trans, JIM 2000;41:1679–82.

[70] Shen B, Kimura H, Inoue A, Mizushima T. Bulk glassy Fe-Co-Ga-P-C-B alloys with high glass-forming ability, high saturation magnetization and good soft magnetic properties. Mater Trans, JIM 2000;41:1675–8.

[71] Shen B-L, Koshiba H, Mizushima T, Inoue A. Bulk amorphous Fe-Ga-P-B-C alloys with a large undercooled liquid region. Mater Trans, JIM 2000;41:873–6.

[72] Shen T, Schwarz R. Bulk ferromagnetic glasses in the Fe-Ni-P-B system. Acta Mater 2001;49:837–47.

[73] Inoue A, Shen B. Soft magnetic bulk glassy Fe-B-Si-Nb alloys with high saturation magnetization above 1.5 T. Mater Trans JIM 2002;43:766–9.

[74] Shen T, Schwarz R. Bulk ferromagnetic glasses prepared by flux melting and water quenching. Appl Phys Lett 1999;75:49–51.

[75] Ponnambalam V, Poon SJ, Shiflet GJ. Fe-based bulk metallic glasses with diameter thickness larger than one centimeter. J Mater Res 2004;19:1320–3.

[76] Lu Z, Liu C, Thompson J, Porter W. Structural amorphous steels. Phys Rev Lett 2004;92:245503.

[77] Inoue A, Kong F, Man Q, Shen B, Li R, Al-Marzouki F. Development and applications of Fe-and Co-based bulk glassy alloys and their prospects. J Alloy Compd 2014;615:S2–8.

[78] Nishiyama N, Takenaka K, Miura H, Saidoh N, Zeng Y, Inoue A. The world's biggest glassy alloy ever made. Intermetallics 2012;30:19–24.

[79] Lou H, Wang X, Xu F, Ding S, Cao Q, Hono K, et al. 73 mm-diameter bulk metallic glass rod by copper mold casting. Appl Phys Lett 2011;99:051910.

[80] Tang M, Zhang H, Zhu Zea FuH, Wang A, Li H, Hu Z. TiZr-base bulk metallic glass with over 50 mm in diameter. J Mater Sci Tech 2010;26:481–6.

[81] Zhang T, Li R, Pang S. Effect of similar elements on improving glass-forming ability of La–Ce-based alloys. J Alloy Compd 2009;483:60–3.

[82] Li R, Pang S, Men H, Ma C, Zhang T. Formation and mechanical properties of (Ce–La–Pr–Nd)–Co–Al bulk glassy alloys with superior glass-forming ability. Scr

Mater 2006;54(6):1123–6.

[83] Zhang Q, Zhang W, Inoue A. Fabrication of new Cu34Pd2Zr48Ag8Al8 bulk glassy alloy with a diameter of 30 mm. Mater Trans, JIM 2007;48:3031–3.

[84] Zheng Q, Xu J, Ma E. High glass-forming ability correlated with fragility of Mg-Cu (Ag)-Gd alloys. J Appl Phys 2007;102:113519.

[85] Guo F, Poon SJ, Shiflet GJ. Metallic glass ingots based on yttrium. Appl Phys Lett 2003;83:2575–7.

[86] Zeng Y, Nishiyama N, Yamamoto T, Inoue A. Ni-rich bulk metallic glasses with high glass-forming ability and good metallic properties. Mater Trans, JIM 2009;50:2441–5.

[87] Schroers J, Johnson WL. Highly processable bulk metallic glass-forming alloys in the Pt-Co-Ni-Cu-P system. Appl Phys Lett 2004;84:3666–8.

[88] Inoue A, Zhang T, Takeuchi A, Zhang W. Hard magnetic bulk amorphous Nd-Fe-Al alloys of 12 mm in diameter made by suction casting. Mater Trans, JIM 1996;37:636–40.

[89] Park E, Kim D. Formation of Ca-Mg-Zn bulk glassy alloy by casting into cone-shaped copper mold. J Mater Res 2004;19:685–8.

[90] Men H, Pang S, Zhang T. Effect of Er doping on glass-forming ability of Co50Cr15Mo14C15B6 alloy. J Mater Res 2006;21:958–61.

[91] Zhang L, Ma E, Xu J. Hf-based bulk metallic glasses with critical diameter on centimeter scale. Intermetallics 2008;16:584–6.

[92] Ji Y, Pang S, Zhang T. Enhanced glass-forming ability of a Sm-based alloy with the addition of La. J Alloy Compd 2010;505:497–500.

[93] Schroers J, Lohwongwatana B, Johnson WL, Peker A. Gold based bulk metallic glass. Appl Phys Lett 2005;87:061912.

[94] Zhao Z, Zhang Z, Wen P, Pan M, Zhao D, Wang WH, et al. A highly glass-forming alloy with low glass transition temperature. Appl Phys Lett 2003;82:4699–701.

[95] Jiao W, Zhao K, Xi X, Zhao D, Pan M, Wang W. Zinc-based bulk metallic glasses. J Non-Cryst Solids 2010;356:1867–70.

[96] Mu J, Fu H, Zhu Z, Wang A, Li H, Hu Z, et al. Synthesis and properties of Al-Ni-La bulk

metallic glass. Adv Eng Mater 2009;11:530–2.

[97] Mahbooba Z, Thorsson L, Unosson M, Skoglund P, West H, Horn T, et al. Additive manufacturing of an iron-based bulk metallic glass larger than the critical casting thickness. Appl Mater Today 2018;11:264–9.

[98] Li H, Lu Z, Yi S. Estimation of the glass forming ability of the Fe-based bulk metallic glass Fe68.8C7.0Si3.5B5.0P9.6Cr2.1Mo2.0Al2.0 that contains non-metallic inclusions. Metal Mater Inter 2009;15:7–14.

[99] Yao K, Zhang C. Fe-based bulk metallic glass with high plasticity. Appl Phys Lett 2007;90.

[100] Kim HK, Lee KB, Lee JC. Ductile Fe-based amorphous alloy. Mater Sci Eng, A 2012;552:399–403.

[101] Park JM, Kim DH, Stoica M, Mattern N, Li R, Eckert J. The influence of in situ formed precipitates on the plasticity of Fe-Nb-B-Cu bulk metallic glasses. J Mater Res 2011;26:2080–6.

[102] Zhao C, Dun C, Man Q, Shen B. Enhancement of plastic deformation in FeCoNbB bulk metallic glass with superhigh strength. Intermetallics 2013;32:408–12.

[103] Park J, Na J, Kim D, Kim K, Mattern N, Kühn U, et al. Medium range ordering and its effect on plasticity of Fe-Mn-B-Y-Nb bulk metallic glass. Phil Mag 2010;90:2619–33.

[104] Shen B, Men H, Inoue A. Fe-based bulk glassy alloy composite containing in situ formed alpha-(Fe, Co) and (Fe, Co)23B6 microcrystalline grains. Appl Phys Lett 2006;89:1915.

[105] Li X, Kato H, Yubuta K, Makino A, Inoue A. Effect of Cu on nanocrystallization and plastic properties of FeSiBPCu bulk metallic glasses. Mater Sci Eng, A 2010;527:2598–602.

[106] Guo S, Liu L, Li N, Li Y. Fe-based bulk metallic glass matrix composite with large plasticity. Scr Mater 2010;62:329–32.

[107] Li X, Kato H, Yubuta K, Makino A, Inoue A. Improved plasticity of iron-based high-strength bulk metallic glasses by copper-induced nanocrystallization. J Non*H.X. Li et al. Progress in Materials Science 103 (2019) 235–318* 309 Cryst Solids 2011;357:3002–5.

[108] Park J, Kim D, Eckert J. Enhanced plasticity of Fe-Nb-B-(Ni, Cu) bulk metallic glasses by controlling the heterogeneity and elastic constants. J Alloy Compd 2012;536:S70–3.

[109] Guo S, Wang J, Zhang H, Xie S. Enhanced plasticity of Fe-based bulk metallic glass by

tailoring microstructure. Trans Nonferrous Met Soc Chin 2012;22:348–53.

[110] Makino A, Li X, Yubuta K, Chang C, Kubota T, Inoue A. The effect of Cu on the plasticity of Fe-Si-B-P-based bulk metallic glass. Scr Mater 2009;60:277–80.

[111] Yang W, Liu H, Zhao Y, Inoue A, Jiang K, Huo J, et al. Mechanical properties and structural features of novel Fe-based bulk metallic glasses with unprecedented plasticity. Sci Rep 2014;4:6233. https://doi.org/10.1038/srep06233.

[112] Gu X, Poon SJ, Shiflet GJ, Widom M. Ductility improvement of amorphous steels: roles of shear modulus and electronic structure. Acta Mater 2008;56:88–94.

[113] Wang J, Li R, Hua N, Huang L, Zhang T. Ternary Fe-P-C bulk metallic glass with good soft-magnetic and mechanical properties. Scr Mater 2011;65:536–9.

[114] Gu X, Poon SJ, Shiflet GJ. Effects of carbon content on the mechanical properties of amorphous steel alloys. Scr Mater 2007;57:289–92.

[115] Guo S, Qiu J, Yu P, Xie S, Chen W. Fe-based bulk metallic glasses: brittle or ductile? Appl Phys Lett 2014;105:161901

[116] Lewandowski J, Wang W, Greer A. Intrinsic plasticity or brittleness of metallic glasses. Phil Mag Lett 2005;85:77–87.

[117] Gu X, McDermott A, Poon SJ, Shiflet GJ. Critical Poisson's ratio for plasticity in Fe-Mo-C-B-Ln bulk amorphous steel. Appl Phys Lett 2006;88:211905.

[118] Gu X, Poon SJ, Shiflet GJ. Mechanical properties of iron-based bulk metallic glasses. J Mater Res 2007;22:344–51.

[119] Lewandowski J, Gu X, Nouri AS, Poon S, Shiflet G. Tough Fe-based bulk metallic glasses. Appl Phys Lett 2008;92:091918.

[120] Liu Y, Wu H, Liu C, Zhang Z, Keppens V. Physical factors controlling the ductility of bulk metallic glasses. Appl Phys Lett 2008;93:151915.

[121] Liu Z, Zhang Z. Mechanical properties of structural amorphous steels: intrinsic correlations, conflicts, and optimizing strategies. J Appl Phys 2013;114:243519.

[122] Chen W, Chan K, Guo S, Yu P. Plasticity improvement of an Fe-based bulk metallic glass by geometric confnement. Mater Lett 2011;65:1172–5.

[123] Wu FF, Zhang ZF, Shen BL, Mao SY, Eckert J. Size effect on shear fracture and fragmentation

of a Fe57.6Co14.4B19.2Si4.8Nb4 bulk metallic glass. Adv Eng Mater 2008;10:727–30.

[124] Wu Y, Li H, Jiao Z, Gao J, Lu Z. Size effects on the compressive deformation behavior of a brittle Fe-based bulk metallic glass. Philos Mag Lett 2010;90:403–12.

[125] Li H, Gao J, Wang S, Yi S, Lu Z. Formation, crystallization behavior, and soft magnetic properties of FeCSiBP bulk metallic glass fabricated using industrial raw materials. Metall Mater Trans A 2012;43:2615–9.

[126] Li Q, Yi S. Improvement of glass forming ability and soft magnetic properties of Fe-C-Si-P amorphous alloys through a flux treatment technique. Metal Mater Inter 2014;20:7–11.

[127] Makino A, Chang C, Kubota T, Inoue A. Soft magnetic Fe-Si-B-P-C bulk metallic glasses without any glass-forming metal elements. J Alloy Compd 2009;483:616–9.

[128] Shen B, Akiba M, Inoue A. Excellent soft-ferromagnetic bulk glassy alloys with high saturation magnetization. Appl Phys Lett 2006;88:131907.

[129] Makino A, Kubota T, Makabe M, Chang CT, Inoue A. Fe-Metalloid metallic glasses with high magnetic flux density and high glass-forming ability. Mater Sci Forum: Trans Tech Publ; 2007. p. 1361–6.

[130] Chang C, Kubota T, Makino A, Inoue A. Synthesis of ferromagnetic Fe-based bulk glassy alloys in the Fe-Si-B-P-C system. J Alloy Compd 2009;473:368–72.

[131] Zhang J, Chang C, Wang A, Shen B. Development of quaternary Fe-based bulk metallic glasses with high saturation magnetization above 1.6 T. J Non-Cryst Solids 2012;358:1443–6.

[132] Kong F, Chang C, Inoue A, Shalaan E, Al-Marzouki F. Fe-based amorphous soft magnetic alloys with high saturation magnetization and good bending ductility. J Alloy Compd 2014;615:163–6.

[133] Meng S, Ling H, Li Q, Zhang J. Development of Fe-based bulk metallic glasses with high saturation magnetization. Scr Mater 2014;81:24–7.

[134] Han Y, Kong F, Chang C, Zhu S, Inoue A, Shalaan E-S, et al. Syntheses and corrosion behaviors of Fe-based amorphous soft magnetic alloys with high-saturation magnetization near 1.7 T. J Mater Res 2015;30:547–55.

[135] Li J-F, Liu X, Zhao S-F, Ding H-Y, Yao K-F. Fe-based bulk amorphous alloys with iron

contents as high as 82 at%. J Magn Magn Mater 2015;386:107–10.

[136] A.O. Olofinjana, H.A. Davies, Mater. Sci. Eng. A 186 (1994) 143.

[137] R. Torres, J.A. Verduzco, Mater. Manuf. Processes 18 (1) (2003) 79.

[138] Xue Li, Hidemi Kato, Kunio Yubuta, Akihiro Makino, Akihisa Inoue. Effect of Cu on nanocrystallization and plastic properties of FeSiBPCu bulk metallic glasses

[139] S.L. Wang, H.X. Li, X.F. Zhang, S. Yi . Effects of Cr contents in Fe-based bulk metallic glasses on the glass forming ability and the corrosion resistance

[140] M.L. Song, D.F.Zhang, X.W.Chen, L.Li. The influence of thermal process on the properties of Fe-based amorphous alloy

[141] H.Liu, L.N.Li, Y.H.Ding, S.S.Zhao, Y.Long. Research on the Effect of Interval Annealing of Iron-based Metallic Glass on Magnetic Properties

[142] Amir Seiffodini, Soheil Zaremehrjardi, Effects of heat treatment on crystallization behavior, microstructure and the resulting microhardness of a (Fe0.9Ni0.1)77Mo5P9C7.5B1.5 bulk metallic glass composite

[143] K. Xu , ZP. Wu , P.Liu, Current Research Status and Prospect of Amorphous Alloys. Materials Research and Application; Volume 15 Issue 4 (2005 / 12 / 01), P30-36

[144] Elham Sharifikolouei, Fabrication of metal microfibers by melt-spinning. DOI: 10.11588/heidok.00028369 Thesis for: PhDAdvisor: Joachim Spatz / Reiner Dahint. January 2018

[145] C. Suryanarayana, A. Inoue, Bulk Metallic Glasses, CRC Press, Boca Raton, London, New York, 2011.

[146] Badis Bendjemil1,2,*, Nasr-eddine Chakri1, Jamal Bougdira3, Enzo Ferrara3, Franco Vinai3, Marcello Baricco4. Crystallization Kinetics and Magnetic Properties of Fe40Ni40B20 Amorphous Ribban.

[147] Anding Wang, Chengliang Zhao, Aina He, Shiqiang Yue, Chuntao Chang, Baolong Shen, Xinmin Wang, Run-Wei Li. Development of FeNiNbSiBP bulk metallic glassy alloys with excellent magnetic properties and high glass forming ability evaluated by different criterions.

[148] Y.R. Zhang, R.V. Ramanujan, J. Alloys Compd. 403 (2005) 197.

[149] A.R. Bhatti, B. Cantor, J. Mater. Sci. 29 (1994) 816.

[150] K. Chrissafis, M.I. Maragakis, K.G. Efthimiadis, E.K. Polychroniadis, J. Alloys Compd. 28 (2004) 375.

[151] K.G. Efthimiadis, E.K. Polychroniadis, S.C. Chadjivasiliou, I.A. Tsoukalas, Mater. Res. Bull. 35 (2000) 937.

[152] K.G. Efthimiadis, G. Stergioudis, S.C. Chadjivasiliou, I.A. Tsoukalas, Cryst. Res. Technol. 37 (2002) 827.

Acknowledgments

I would like to thank my supervisors Prof. Monica Ferraris and Dr. Elham Sharifikolouei; it has been an honor working with them during 6 months of work, and they give me a lot of help and support for analyzing experimental data and calibration methodologies.

I am also grateful to my parents, Mr. Xing Jinlong and Mrs. Shi Zuoxia, for their great encouragement and support during my study abroad.